



HAL
open science

Experiments on symmetry breaking of azimuthal combustion instabilities and their analysis combining acoustic energy balance and flame describing functions

V. Latour, D. Durox, Antoine Renaud, S. Candel

► To cite this version:

V. Latour, D. Durox, Antoine Renaud, S. Candel. Experiments on symmetry breaking of azimuthal combustion instabilities and their analysis combining acoustic energy balance and flame describing functions. *Journal of Fluid Mechanics*, 2024, 985, pp.A31. <10.1017/jfm.2024.307>. <hal-05233947>

HAL Id: hal-05233947

<https://centralesupelec.hal.science/hal-05233947v1>

Submitted on 1 Sep 2025

HAL is a multi-disciplinary open access archive for the deposit and dissemination of scientific research documents, whether they are published or not. The documents may come from teaching and research institutions in France or abroad, or from public or private research centers.

L'archive ouverte pluridisciplinaire HAL, est destinée au dépôt et à la diffusion de documents scientifiques de niveau recherche, publiés ou non, émanant des établissements d'enseignement et de recherche français ou étrangers, des laboratoires publics ou privés.



Distributed under a Creative Commons CC BY 4.0 - Attribution - International License

Banner appropriate to article type will appear here in typeset article

1 Experiments on symmetry breaking of azimuthal 2 combustion instabilities and their analysis 3 combining acoustic energy balance and flame 4 describing functions

5 V. Latour¹ †, D. Durox¹, A. Renaud¹, and S. Candel¹

6 ¹Laboratoire EM2C, CNRS, CentraleSupélec, Université Paris-Scalay, 3, rue Joliot Curie, 91192
7 Gif-sur-Yvette cedex, France

8 (Received xx; revised xx; accepted xx)

9 Combustion instabilities in annular systems raise fundamental issues that are also of practical
10 importance to aircraft engines and ground-based gas turbine combustors. Recent studies
11 indicate that the injector plays a significant role in the stability of combustors by defining
12 the flame dynamical response and setting the inlet impedance of the system. The present
13 investigation examines the effects of combinations of injectors of two different types (U and
14 S) on thermo-acoustic instabilities in a laboratory-scale annular combustor and compares
15 different circumferential staging strategies. The combustor operates in a stable fashion when
16 all injection units belong to the S-family but exhibits large amplitude pressure oscillations
17 when all these units are of the U-type. When the system comprises a mix of U and S
18 injectors, it is possible to determine the number of S-injectors leading to stable operation.
19 For a fixed proportion of U and S-injectors, some arrangements give rise to stable operation
20 while others do not. Results also show that introducing symmetry-breaking elements affects
21 the system's modal dynamics. These experimental observations are interpreted in an acoustic
22 energy balance framework used to derive an expression for the growth rate as a function of
23 the describing functions of the flames formed by the different injectors and their respective
24 azimuthal locations. Growth rates are determined for the different configurations and used to
25 explain the various observations, estimate the system damping rate, and predict the location
26 of the nodal line when the standing mode prevails.

27 **Key words:** Combustion, acoustics, instabilities

28 1. Introduction

29 Thermo-acoustic instabilities result from a constructive coupling between the acoustics of
30 the system and the combustion process. On the fundamental level, these phenomena raise
31 many scientific issues concerning the driving processes, the coupling mechanisms, and their
32 reduced-order modeling. In practice, these instabilities give rise to large amplitude pressure

† Email address for correspondence: veranika.latour@centralesupelec.fr

2

33 oscillations that sometimes reach levels of a few percent of the mean chamber pressure,
34 producing intense heat release rate fluctuations in the combustion system and submitting its
35 structure and components to enhanced vibrations and thermal loads. These phenomena can
36 lead to cyclic fatigue and cause severe damage to the combustion chamber, eventually leading
37 to the mechanical failure of the system (Candel (2002), Huang & Yang (2009), Poinso
38 (2017)).

39 Much of the research effort in this field is currently focused on instabilities in high
40 performance devices and in particular in gas turbine combustors. These devices are in most
41 cases annular, and in this geometry, instabilities can be coupled by axial and azimuthal
42 modes. The azimuthal modes are generally considered to be the most dangerous because
43 they are less well damped and their eigenfrequencies, determined by the perimeter of the
44 chamber (which is the largest dimension of the system), lie in the low frequency range
45 where the flames are most susceptible to disturbances. An intensive research effort has
46 been carried out through theoretical analysis (Evesque & Polifke (2002), Parmentier *et al.*
47 (2012), Noiray & Schuermans (2013), Ghirardo & Juniper (2013), Campa & Camporeale
48 (2014), Bothien, Noiray & Schuermans (2015)), experiments (Krebs *et al.* (2002), Kopitz
49 *et al.* (2005), Fanaca *et al.* (2008), Worth & Dawson (2013), Bourgouin *et al.* (2013),
50 Prieur *et al.* (2017), Rajendram Soundararajan *et al.* (2021), Indlekofer *et al.* (2022)) and
51 numerical simulations (Pankiewicz & Sattelmayer (2003), Staffelbach *et al.* (2009), Wolf
52 *et al.* (2012)) to better understand the physical phenomena at stake and more reliably predict
53 thermo-acoustic oscillations at an early stage of the combustor design process.

54 The present article aims to provide further insights into the coupling giving rise to
55 azimuthal instabilities in annular combustors. This is achieved by making use of systematic
56 experimentation. The central idea is to use two families of injection units that give rise to
57 flames with notably different dynamical characteristics and consider various combinations of
58 these units to examine the dynamics of the annular combustor, the transition between unstable
59 and stable operation, analyze the modal structure that couples self-sustained oscillations and
60 identify implications in terms of symmetry breaking. A second objective of this article is
61 to propose an interpretation of these data using an analytical framework combining acoustic
62 energy balance principles and measured flame describing functions.

63 Since the present article investigates symmetry breaking induced by mixing different types
64 of injection units, it is natural to stress their role in combustion instabilities arising in swirl-
65 stabilized combustors. First, these units influence the acoustics of the system through the
66 impedance they impose at the inlet of the combustion chamber (Fischer *et al.* (2006), Huang
67 & Yang (2009), Rajendram Soundararajan *et al.* (2022*b*)). Second, the injection system
68 determines the swirl number, flow pattern, spray geometry and droplet size distribution which
69 essentially define the flame structure, the heat release rate distribution, and consequently
70 the flame dynamics, i.e. the flame's response to acoustic disturbances, that is commonly
71 characterized by flame describing functions. Large eddy simulations carried out by Huang
72 & Yang (2005) reveal the effect of inlet swirl on flow pattern and combustion dynamics.
73 Experiments indicate that flame dynamics is notably influenced by the axial position of the
74 swirl generator (Komarek & Polifke (2010)) and the injection unit pressure drop and swirl
75 number (Vignat *et al.* (2019), Rajendram Soundararajan *et al.* (2022*a*)).

76 Annular combustors feature a rotational symmetry when identical injection units are
77 regularly spaced around the circumference of the annulus. Symmetry breaking and staging
78 concepts (introduction of asymmetry in the annular system by mixing injectors presenting
79 different characteristics) have been the subject of theoretical, numerical, and experimental
80 investigations to assess the suitability of these strategies to reduce and control thermo-acoustic
81 instabilities coupled by azimuthal modes.

82 Noiray, Bothien & Schuermans (2011) examined circumferential staging by testing

83 configurations mixing two types of burners using a theoretical framework and thermo-
84 acoustic network simulations. Analytical expressions derived from dynamic system theory
85 enable to identify a bifurcation parameter, which in the case of an unstable n -th azimuthal
86 mode, is the $2n$ component of the Fourier expansion of the azimuthal distribution of flame
87 transfer functions. The value of this parameter defines the nature of the unstable mode
88 encountered in the annular configuration: standing, spinning, or mixed. The analysis is
89 pursued by Ghirardo & Juniper (2013) to include effects of transverse excitation of the
90 flames and by Bothien, Noiray & Schuermans (2015) who consider the circumferential
91 staging effect due to different flame responses. Parmentier *et al.* (2012) developed an
92 analytical model and investigated symmetry breaking in the case of an annular system
93 with four burners, where two types of burners are mixed. It was shown in that study that
94 passive control of azimuthal instabilities is more effective when burners of the same type
95 are located side by side and not when they are disposed symmetrically. Bauerheim *et al.*
96 (2014) extended this analytical approach to an annular system with N identical or non-
97 identical burners. Two parameters affecting the stability of the system were highlighted: the
98 coupling strength, corresponding to the cumulative effects of the N flames, which controls
99 the stability at first order, and the splitting strength, resulting from symmetry breaking when
100 the flames are different, which affects the nature of the mode. The model also shows that
101 mixing two types of injectors promotes non-degenerate modes and favours the occurrence
102 of standing modes. More recent additions to the literature pursue the theoretical analysis of
103 symmetry breaking using uncertainty quantification (Bauerheim *et al.* (2016)) or the adjoint
104 perturbation framework (Mensah *et al.* (2019)).

105 On the experimental level, the effects of asymmetric power distribution in an annular Rijke
106 tube arrangement were investigated by Moeck, Paul & Paschereit (2010) through azimuthal
107 variations of the electrical power supplied to each heating grid. Different unstable modes are
108 found, and the influence of heating distribution on the damping of instabilities is analyzed.
109 More recently, Humbert *et al.* (2023) examined the effects of symmetry breaking on the
110 degeneracy and nature of azimuthal thermoacoustic modes of an annular combustor model
111 with electroacoustic feedback. Aguilar *et al.* (2021) showed the effects of symmetry breaking
112 on the location of the pressure anti-nodal line in the MICCA annular chamber equipped with
113 laminar matrix burners. Symmetry breaking was achieved by partially blocking the holes of
114 some matrix burners. It was found that, if the expected oscillation for the operating point in
115 the symmetrical situation is a standing mode, the introduction of symmetry breaking favours
116 this mode type and the position of the nodal line locks in the region where the symmetry
117 breaking elements are located. When the expected mode in the symmetrical configuration
118 is of the spinning type, symmetry breaking does not lead to the appearance of a standing
119 mode, indicating, according to the authors, that the symmetry breaking had to be stronger to
120 change the nature of the mode. The effects of symmetry breaking on the modes in annular
121 combustors and nodal line locking are discussed further in section 3.3.

122 In addition to “geometrical symmetry breaking” (mixing injectors with different charac-
123 teristics), Bauerheim, Cazalens & Poinsot (2015) analyzed the case of “flow symmetry
124 breaking”, resulting from a mean swirling motion in the annular system, which splits
125 azimuthal modes into two waves having unequal but close frequencies and structures.
126 Compared to the degenerate modes prevailing in the absence of mean azimuthal flow, the
127 spinning mode is favoured. Humbert *et al.* (2021) imposed a mean tangential flow in an
128 annular system equipped with electro-acoustic actuators and observed the formation of beats
129 due to the degeneracy loss of the acoustic mode, resulting from the small frequency difference
130 between the clockwise and counterclockwise travelling waves.

131 Introducing Helmholtz resonators or baffles in an annular system constitutes another
132 means of symmetry breaking. An analytical investigation of the best placement of Helmholtz

4

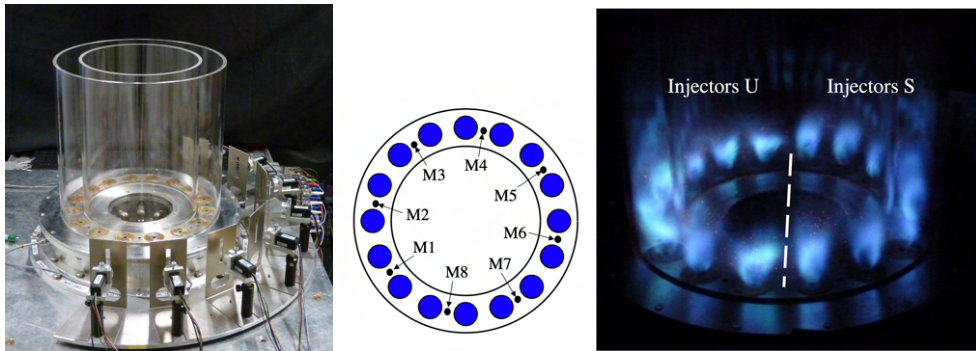


Figure 1: Left: the MICCA-Spray test rig and array of the eight photomultipliers used to measure OH* emission from the flames (these sensors are employed in section 4.2 and Appendix C). Center: top view of MICCA-Spray and microphones positions (center). Right: MICCA-Spray equipped with 8 U-injectors placed on one half of the annulus and 8 S-injectors on the other half. The white dashed line separates U and S injection units.

133 resonators for the damping of azimuthal instabilities in an annular system can be found
 134 in Stow & Dowling (2003), and the authors showed that Helmholtz resonators introduce
 135 circumferential mode coupling. The damping effect of baffles number and position on thermo-
 136 acoustic instabilities in an annular combustor was experimentally studied by Dawson & Worth
 137 (2015). The authors report that even if no damping was observed with a single baffle, the
 138 azimuthal symmetry is broken, leading to a coupling between the counterclockwise (CCW)
 139 and clockwise (CW) azimuthal waves, promoting a standing mode.

140 The present article proposes to investigate circumferential staging by examining config-
 141 urations mixing two types of injection units that were recently found to belong to distinct
 142 categories with different flame dynamics, namely low-swirl moderate-pressure drop and
 143 high-swirl high-pressure drop units (Rajendram Soundararajan *et al.* (2022a)). Injectors of
 144 the former category (denoted “707” in the last reference but referred to as “S-injectors” in
 145 what follows) were found to lead to stable operation in MICCA-Spray, whereas others (“U-
 146 injectors”, denoted “727” in the last reference) led to unstable oscillations over a relatively
 147 broad operating domain (thermal power from 93 to 118 kW and global equivalence ratio
 148 between 0.75 and 1.05). In the same range of operation, different arrangements of U- and
 149 S-injectors are examined in the present study and the experimental results are interpreted
 150 using an analytical framework derived from acoustic energy balance equations and used to
 151 evaluate the growth rate. The key idea is to identify the contribution of the different flames
 152 to the global energy source term of the system by making use of an analytical expression of
 153 the source term depending on the injection units’ azimuthal location in the system and on
 154 flame describing functions, here experimentally determined in a single-sector configuration,
 155 designated as SICCA-Spray.

156 After a presentation of the annular combustor MICCA-Spray and the injectors’ charac-
 157 teristics (section 2), different arrangements of U- and S-injectors are tested (section 3).
 158 Systematic experiments indicate that the number of S-injectors changes the level of pressure
 159 fluctuations in the system, and for a given number of S-injectors in the system, their relative
 160 position also has a notable influence, not only on the level of pressure fluctuations, but also
 161 on modal dynamics and the nodal line location. A theoretical framework based on acoustic
 162 energy balance equations and flame describing functions is derived in section 4 to interpret
 163 the experimental observations through the determination of the growth rates for the different
 164 configurations and estimate the damping rate in the annular system.

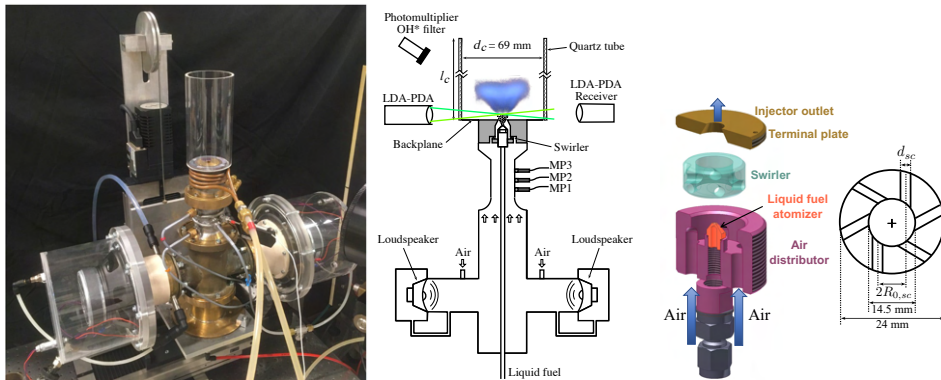


Figure 2: The SICCA-Spray setup (left), SICCA-Spray configuration for FDF measurements (center), and exploded view of the injector along with a top view of the swirler (right).

165 2. Experimental setup, injector characteristics and modal identification

166 The MICCA-Spray annular combustor is first presented. Then, the characteristics of the two
 167 types of injector used in this study are compared, based on their flame describing functions,
 168 measured in the single-sector configuration, SICCA-Spray. Finally, sections 2.3 and 2.4
 169 describe the acoustic mode structures that can be observed in annular systems and the modal
 170 identification procedure.

171 2.1. The MICCA-Spray annular system

172 The MICCA-spray annular combustion chamber, shown in Fig. 1, is formed by two quartz
 173 walls of the same length, $l = 400$ mm, of outer diameter 300 mm for the inner cylinder, and
 174 inner diameter 400 mm for the outer quartz cylinder. The backplane comprises 16 regularly
 175 spaced injection units, which deliver liquid fuel, heptane in the present experiments, as a
 176 hollow cone spray of droplets mixed with air (Vignat *et al.* (2021)). The air mass flow
 177 rate is controlled through two Bronkhorst EL-FLOW mass flow meters and the fuel mass
 178 flow rate through a Bronkhorst CORI-flow mass flow rate controller. Eight Brüel & Kjær
 179 microphones, flush-mounted on waveguides to protect them from the hot gas temperature
 180 environment, enable to record pressure fluctuations at the combustion chamber backplane,
 181 with a sampling frequency $f_s = 32\,768$ Hz.

182 The stability maps of MICCA-Spray equipped with these two types of injectors are
 183 presented by Rajendram Soundararajan *et al.* (2022a). In that reference, as already mentioned,
 184 “injector S” is denoted “707” and “injector U”, “727”. The operating point chosen for the
 185 present study corresponds to a thermal power value $\mathcal{P} = 118$ kW and a global equivalence
 186 ratio $\phi = 0.9$. Under these conditions, the chamber is unstable when it is equipped with
 187 U-injectors and stable when it is equipped with S-injectors.

188 2.2. Injector characteristics and flame describing functions

189 An exploded view of the injection units used in this study is presented in Fig. 2 (c). These
 190 injectors are composed of four main elements: an air distributor, a liquid fuel atomizer, a
 191 swirler, and a terminal plate with a convergent nozzle. Changing the swirler changes the swirl
 192 number and pressure drop through the injection unit.

193 The characteristics of injectors U and S (swirl number, pressure drop, and pressure drop
 194 coefficient) are gathered in Tab. 1. Injector S presents a lower swirl number and a lower
 195 pressure drop value than injector U.

Injector	S_N	Δp (kPa)	σ
Injector S (stable in MICCA-Spray)	0.60	3.65	3.33
Injector U (unstable in MICCA-Spray)	0.74	5.70	5.20

Table 1: Injector characteristics: swirl number (S_N), pressure drop (Δp), and pressure drop coefficient (σ), obtained from measurements under cold conditions for an air mass flow rate of 2.3 g s^{-1} (Vignat *et al.* (2021)).

196 It is also interesting to examine the effects of the injector characteristics on flame dynamics
 197 through the measurement of flame describing functions (FDFs). FDFs characterize the
 198 response of flames to acoustic disturbances and the FDF framework (Dowling (1997),
 199 Noiray *et al.* (2008)), which is the nonlinear extension of flame transfer functions, is now
 200 widely used in combustion system stability analysis. They enable to capture saturation effects
 201 on the flame response and explain nonlinear phenomena such as triggering, mode hopping or
 202 hysteresis. FDFs are the subject of theoretical investigations (Ghirardo *et al.* (2015), Orchini,
 203 Illingworth & Juniper (2015)) and are commonly used as an input in reduced-order models
 204 to interpret experimental observations (Schuermans *et al.* (2010), Paliès *et al.* (2011), Han,
 205 Li & Morgans (2015), Schuller, Poinso & Candel (2020)).

206 FDF measurements are carried out in a single-injector configuration, SICCA-Spray,
 207 displayed in Fig. 2, representing one sector of the annular system MICCA-Spray. The system
 208 can be modulated from the upstream side of the injector by two driver units placed at
 209 the bottom of the plenum and connected to a sinewave generator. The operating point in
 210 SICCA-Spray is chosen so that it corresponds to the thermal power value of one injector in
 211 MICCA-Spray, that is to say 1/16th of the total thermal power in MICCA-Spray.

212 With the type of injectors used, equivalence ratio fluctuations are small compared to
 213 velocity fluctuations, so that the flame behaves in a quasi-premixed fashion (Rajendram
 214 Soundararajan *et al.* (2022b)). FDFs are thus defined as the ratio of relative heat release rate
 215 fluctuations to relative volume flow rate fluctuations

$$216 \quad \mathcal{F}(f, q') = \frac{\dot{Q}'/\bar{\dot{Q}}}{q'/\bar{q}} = G(f, q')e^{i\varphi(f, q')} \quad (2.1)$$

217 Relative heat release rate fluctuations are measured with a photomultiplier equipped with
 218 a OH* filter centred at 310 nm. The injector being weakly transparent to acoustic waves,
 219 velocity fluctuations measured upstream of the injector are not the same as those measured
 220 on its downstream side. Hence velocity fluctuations are measured with a Laser Doppler
 221 Anemometry Dantec Dynamics system, in the combustion chamber, at a position ($z = 2.5$
 222 mm above the backplane and at $r = 3.5$ mm from the center for injector S and at $r = 4.0$ mm for
 223 injector U) where relative velocity fluctuations match relative volume flow rate fluctuations,
 224 to comply with the FDF definition (Rajendram Soundararajan *et al.* (2022b)). The fuel
 225 droplets, featuring a mean diameter below $5 \mu\text{m}$ at the measurement positions, can serve as
 226 flow tracers in the frequency range of interest (250 to 850 Hz). Measurements are carried out
 227 for seven levels of modulation amplitudes, corresponding to different voltage outputs of the
 228 sinewave generator, and leading to different values of relative velocity fluctuations depending
 229 on the frequency and the level of the modulation amplitude.

230 FDFs measured in SICCA-Spray equipped with injectors U and S are displayed in Fig.
 231 3. FDF gain values are substantially lower for injector S than for injector U, and this is
 232 particularly true in a range of frequencies around 800 Hz, close to the eigenfrequency of

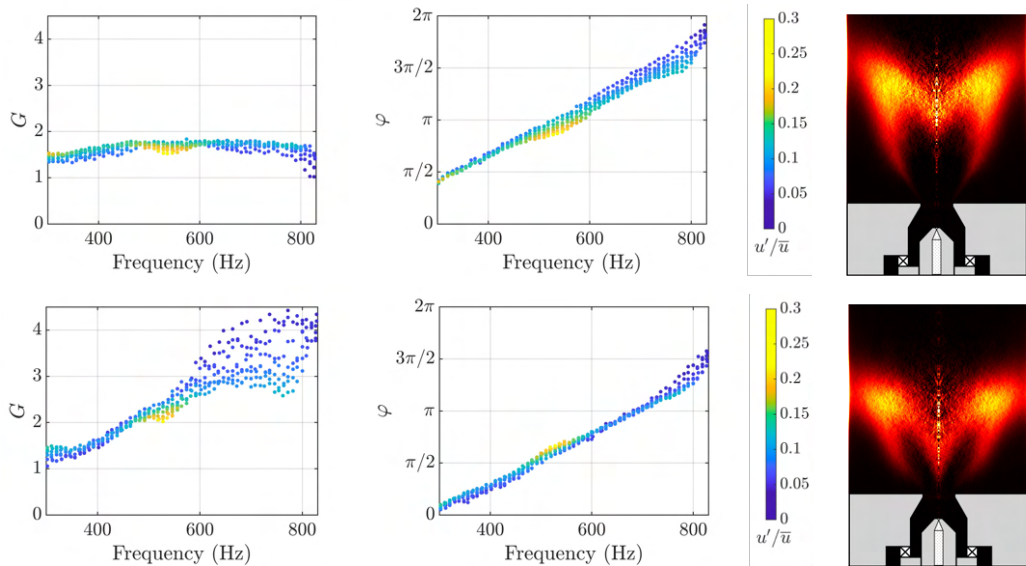


Figure 3: Flame describing function gain and phase (first and second columns respectively) and OH^* chemiluminescence distributions obtained after Abel inversion of the average images recorded by an intensified CCD camera, under stable operation in SICCA-Spray (third column): S-injector (top), U-injector (bottom).

233 the 1A1L (1st azimuthal- 1st longitudinal) mode of the MICCA-Spray annular combustion
 234 chamber, involved in the combustion/acoustics coupling, as will be detailed in the next
 235 section. Differences in phases are also observed, with higher phase values for injector S
 236 than injector U in the range of frequencies investigated. Figure 3 also displays flame images
 237 obtained from the Abel inversion of the images captured with a CCD camera, to show the
 238 effect of the injector pressure drop and swirl number on the flame shape. The “V” shaped
 239 flame obtained with injector S is longer and narrower than that obtained with injector U, a
 240 hollow “M” shape flame which is more compact, due to a higher swirl number of the injection
 241 unit.

242 Another effect that deserves to be considered is that injectors U and S have different
 243 pressure drop coefficients. When these injectors are mixed in various proportions, the air
 244 flow velocities through these units will not be the same, and since the mass flow rate of fuel
 245 is unaffected, the equivalence ratios will also differ for the two types of injectors and their
 246 operating point will be shifted with respect to the case where all injection units are the same.
 247 Calculations reported in Appendix A indicate that the operating point for U-injectors are
 248 shifted towards higher equivalence ratio values, while those of S-injectors change towards
 249 lower values and that the changes depend on the number of U and S injectors. It is shown
 250 however in Appendix A, through FDF measurements for different equivalence ratio values,
 251 that the variations encountered in this study only have a slight effect on the FDF gain and
 252 phase values, and hence on the flame dynamics of the individual flames.

253

2.3. Modal structures and frequencies

254 At this point it is worth briefly describing the acoustic mode structures that can be observed
 255 in annular systems, specify those that are effectively observed experimentally, and obtain
 256 an estimate of the corresponding eigenfrequencies. In the present configuration, the annulus
 257 mean radius R is large compared to the width of the annulus and one may neglect any

8

258 radial variation. Then, the large ratio between the surface area of the backplane and that
 259 of the injector outlet induces a decoupling of the plenum and the combustion chamber: the
 260 combustion chamber modes are weakly influenced by the plenum acoustics, as shown by
 261 Schuller *et al.* (2012), where conditions on temperatures and area ratios to obtain decoupled
 262 cavities are discussed. Furthermore, the injectors used are weakly transparent to acoustic
 263 waves, accentuating the decoupling (Rajendram Soundararajan *et al.* (2022b), Latour *et al.*
 264 (2023b)). The chamber backplane hence acts like a rigid wall and the exhaust is open to
 265 the atmosphere. In this configuration, the acoustic coupling modes are of the mixed axial-
 266 azimuthal type and may be designated by mA,nL . The pressure field can be cast in the
 267 following form:

$$268 \quad \tilde{p}_{mn}(x, \theta, t) = [A_{mn}^+ \exp(im\theta - i\omega_{mn}t) + A_{mn}^- \exp(-im\theta - i\omega_{mn}t)]\psi_n(x) \quad (2.2)$$

269 In this expression, m and n are integers, with $m \geq 0$ and $n \geq 1$, θ is the azimuthal
 270 angle considered positive in the counterclockwise (CCW) direction, and ω_{mn} is the angular
 271 frequency. The amplitudes A_{mn}^+ and A_{mn}^- correspond to counterclockwise and clockwise
 272 (CW) spinning waves respectively, and $\psi_n(x)$ is the axial wavefunction satisfying the
 273 boundary conditions on the chamber backplane and at its exhaust. In the present case,
 274 the backplane is rigid and the outlet is open to the atmosphere, i.e. corresponds to a pressure
 275 node (in fact the pressure does not quite vanish at the outlet but at a short distance from that
 276 section, and this may be accommodated by adding an end correction δ_a to the length of the
 277 chamber and replacing this length by $l' = l + \delta_a$). The longitudinal eigenfunctions are in this
 278 case: $\psi_n(x) = \cos[(2n - 1)\pi x / (2l')]$. The eigenfrequencies corresponding to the previous
 279 modes are then given by a standard expression

$$280 \quad f_{mn} = \left[m^2 \left(\frac{c}{\mathcal{P}_a} \right)^2 + (2n - 1)^2 \left(\frac{c}{4l'} \right)^2 \right]^{1/2} \quad (2.3)$$

281 where $\mathcal{P}_a = 2\pi R$ is the mean perimeter of the system, and c , the speed of sound. In all
 282 the present experiments, one observes the 1A1L mode corresponding to $m = 1$ and $n = 1$,
 283 and one may simplify the notations by neglecting the indices m and n in the pressure field
 284 expression

$$285 \quad \tilde{p}(x, \theta, t) = [A^+ \exp(i\theta - i\omega t) + A^- \exp(-i\theta - i\omega t)]\psi(x) \quad (2.4)$$

286 It is worth mentioning that this expression of the pressure field does not capture nearfield
 287 modifications associated with the flames. One may also think that the purely azimuthal
 288 structure will be perturbed by the different staging patterns. However, these effects are
 289 expected to be small and this is confirmed by experimental measurements of the annular
 290 distributions of pressure signals as will be seen later on. Thus, Eq. 2.4 constitutes a reasonable
 291 approximation of the pressure field.

292 Finally, the eigenfrequency of this mode writes

$$293 \quad f_{11} = \left[\left(\frac{c}{\mathcal{P}_a} \right)^2 + \left(\frac{c}{4l'} \right)^2 \right]^{1/2} \quad (2.5)$$

294 It is now worth estimating the resonant frequency using the last expression. In the MICCA-
 295 Spray experiments, the perimeter $\mathcal{P}_a \simeq 1.1$ m. The end correction for an annular system
 296 is not well known theoretically but some pressure measurements near the chamber exhaust
 297 indicate that $\delta_a \simeq 0.09$ m so that $l' \simeq 0.49$ m. Assuming an average temperature in the
 298 chamber $T \simeq 1500$ K, defining a speed of sound $c = 761$ m/s, the eigenfrequency of the
 299 1A1L mode is $f_{11} \simeq 808$ Hz. We will see that this value is close to the peak frequencies
 300 observed experimentally, indicating that the coupling mode is essentially defined in this setup
 301 by the combustion chamber modes and that most oscillations are of the 1A1L type.

302 For more complex geometries (for example in the case of a coupling between the

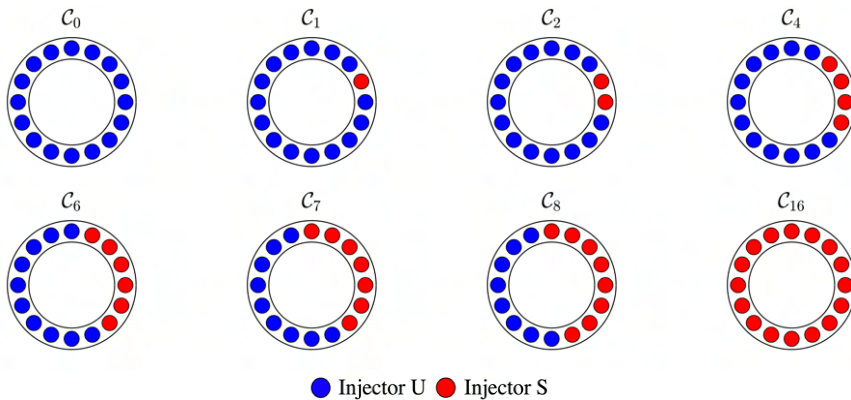


Figure 4: “Side-by-side” (type C) configurations investigated.

303 plenum and the combustion chamber), the eigenfrequencies of the modes involved in the
 304 combustion/acoustics coupling can be found using a Helmholtz solver, where the geometry
 305 and temperatures in the various cavities can be specified (Bourgouin *et al.* (2013)). It is
 306 important to stress that the presence of the flame acting as an unsteady heat release source
 307 modifies the resonant loop, possibly shifting the oscillation frequency of the system with
 308 respect to the modal eigenfrequency (Durox, Schuller, & Candel (2002), Schuller, Poinso
 309 & Candel (2020)). However, the acoustic method exposed previously provides a reasonable
 310 first approximation of the thermo-acoustic oscillation frequency, which can then be refined
 311 with a perturbation/correction procedure.

312

2.4. Modal identification

313 The signals recorded by the eight waveguided microphones plugged on the chamber
 314 backplane can be used to determine the frequency of oscillation of the modes coupling the
 315 instability. The peak frequency is obtained from the power spectral density (PSD) of these
 316 microphone signals. The PSD is calculated using Welch’s method applied to 63 blocks of
 317 8192 samples with a 50% overlap and a Hamming window weighting. With these parameters,
 318 the frequency resolution is $\Delta f = 4$ Hz. For all the unstable configurations investigated, the
 319 power spectral densities, which will be discussed further in Sec. 4.3, only feature a main peak
 320 at the fundamental frequency. Cases leading to non-degenerate modes characterized by close
 321 eigenfrequencies, which difference is below the resolution frequency, will also be examined.

322 The complex wave amplitudes A_+ and A_- may be retrieved from the eight microphone
 323 signals by solving an overdetermined system of linear equations using a least squares
 324 algorithm. One may then deduce the instability amplitude

$$325 \quad A = [(A^+)^2 + (A^-)^2]^{1/2} \quad (2.6)$$

326 which corresponds to a value averaged in time and space, and is independent of the instability
 327 mode.

328 3. Experimental results

329 Different arrangements of injectors U and S are now investigated. It is logical to begin
 330 with a configuration equipped with 16 U-injectors and then observe what happens when
 331 one successively introduces one to eight S-injectors in “side-by-side” arrangements, where
 332 all the S-injectors are gathered on the same side of the annulus. One may then see how

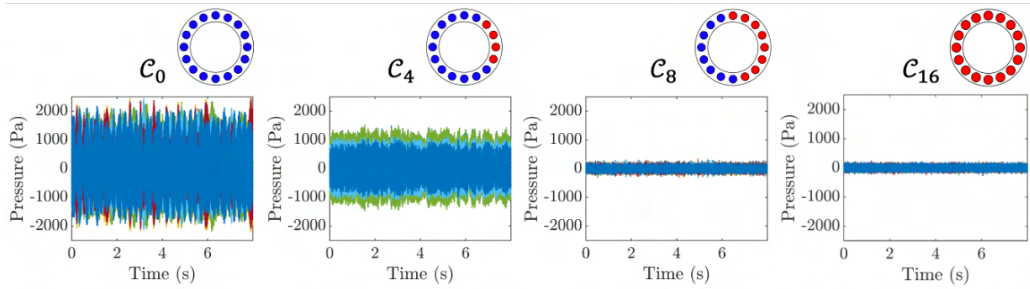


Figure 5: Pressure time series in the MICCA-Spray annular combustor for 4 configurations (from left to right): C_0 , C_4 , C_8 , and C_{16} . Experiments are carried out at a thermal power $\mathcal{P} = 118$ kW and a global equivalence ratio $\phi = 0.9$.

333 many U-injectors have to be replaced by S-injectors to completely damp the instability. In
 334 a second step, the number of S-injectors is fixed and different positions for S-injectors are
 335 tested to examine how the relative position of S and U-injectors impacts the level of pressure
 336 fluctuations in the system. In the last subsection, the effect of circumferential staging on the
 337 modal dynamics of the system is investigated.

338

3.1. Side-by-side arrangements of S injectors

339 A first category of arrangements is investigated and will be referred to as “C arrangements”.
 340 N_s S-injectors are placed side-to-side, with N_s ranging from 0, corresponding to the case
 341 where there are no S injectors in the system, to $N_s = 8$, where half of the injectors is of
 342 the U type while the other half is of the S type. Pressure traces are also presented for a
 343 configuration comprising 16 S-injectors ($N_s = 16$) to complete the comparison. The eight
 344 investigated arrangements of this kind are displayed in Fig. 4.

345 Pressure times series for $N_s = 0, 4, 8$ and 16 are displayed in Fig. 5. When $N_s = 0$, the
 346 combustor exhibits high pressure fluctuation levels, and when 16 S-injectors are mounted
 347 ($N_s = 16$), the system operates in a stable fashion. Replacing an increasing number of U-
 348 injectors by S injectors diminishes the level of pressure fluctuations in the chamber. When
 349 $N_s = 8$, pressure oscillations reach levels similar to those recorded in configuration C_{16}
 350 (around 100 Pa).

351 Figure 6 shows the level of pressure fluctuations in the chamber and the frequency of the
 352 instability as a function of the number of S-injectors. A gradual decrease in the pressure
 353 level is observed as N_s is increased. If one now looks at the frequencies, the values found
 354 are around 800 Hz, indicating that the mode involved in the combustion/acoustics coupling
 355 is the 1A1L mode of the annular chamber. The instability frequency decreases from 820 Hz
 356 to 790 Hz as the number of S-injectors in the chamber is augmented. The presence of the
 357 flames shifts the frequencies with respect to the eigenfrequency of the system without flames
 358 (which in this case was estimated to be 808 Hz for the 1A1L mode by taking a burnt gas
 359 temperature $T = 1500$ K). The change in frequency with the number of S-injectors in the
 360 system reflects modifications in the combustion/acoustics coupling linked to a progressively
 361 weaker combustion response as the number of S-injectors, characterized by FDFs that differ
 362 from that of U-injectors, is increased. This might also possibly be explained by a non-uniform
 363 azimuthal temperature distribution associated with the variation in equivalence ratio values
 364 due to the introduction of S injectors in the system.

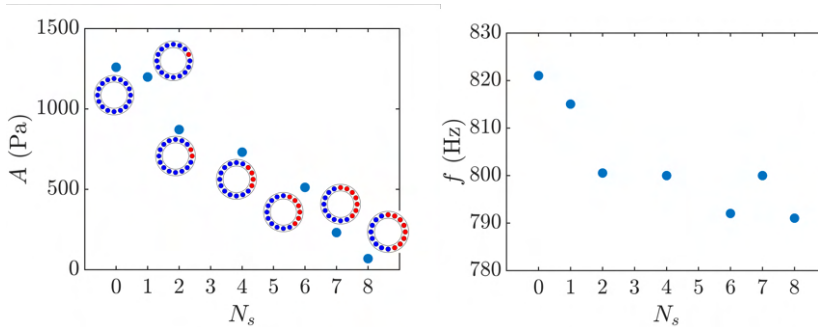


Figure 6: Instability amplitude (left) and frequency (right) as a function of the number N_s of S-injectors in MICCA-Spray for type C configurations. Experiments are carried out at a thermal power $\mathcal{P} = 118$ kW and a global equivalence ratio $\phi = 0.9$.

365

3.2. Effects of the S-injectors azimuthal locations

366 In what follows, the number of S-injectors is fixed, and the effects of the relative position of
 367 these units are investigated by considering arrangements with 2, 4, 6, and 8 S-injectors. A first
 368 group of arrangements shown in Fig. 7 (top), denoted \mathcal{L}_2 , \mathcal{L}_4 , \mathcal{L}_6 , and \mathcal{L}_8 , corresponds to
 369 cases where the S-injectors are divided into two groups of equal size and placed on opposite
 370 sides of the annulus. For $N_s = 4$ and $N_s = 8$, a second category of arrangements, shown in
 371 Fig. 7, bottom, is also investigated, and will be denoted \mathcal{A}_4 and \mathcal{A}_8 to designate an alternation
 372 of U and S-injectors.

373 Figures 8 and 9 show the arrangements investigated together with the pressure time series.
 374 These two figures indicate that, for a given number of S-injectors, “face-to-face” (type \mathcal{L})
 375 arrangements lead to higher levels of pressure fluctuations than “side-by-side” (type C)
 376 arrangements. In this respect, the case with 8 S-injectors is particularly interesting (Fig. 8,
 377 bottom). Arrangements where the 8 S-injectors are gathered on one side of the chamber (\mathcal{C}_8)
 378 or for which there is an alternation between injectors S and U (\mathcal{A}_8) lead to stable operation
 379 while arrangement \mathcal{L}_8 induces large amplitude oscillations, with pressure fluctuations levels
 380 similar to those recorded in the cases without S-injectors. For configurations with 4 S-
 381 injectors in the system (Fig. 9, bottom), arrangement \mathcal{A}_4 enables a more efficient reduction
 382 of the oscillations amplitude than \mathcal{C}_4 .

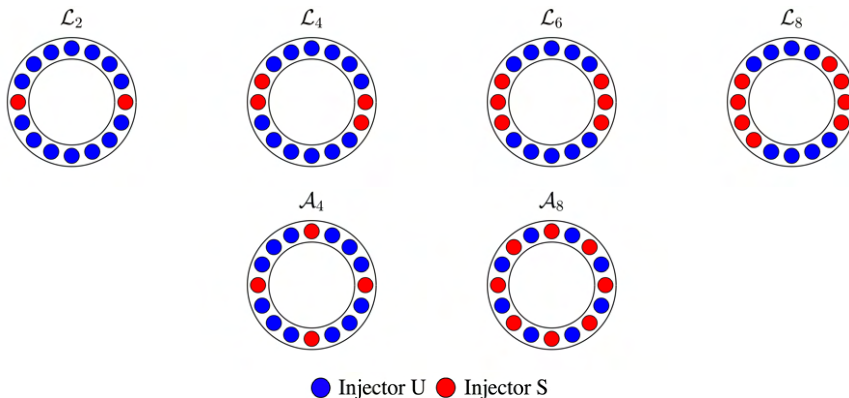
383 Figure 10 shows the amplitude of pressure fluctuations and the instability frequency as
 384 a function of the number of S-injectors for all the configurations tested. Compared to C
 385 configurations, \mathcal{L} arrangements lead to a level of pressure fluctuations in the chamber higher
 386 than or very close to the reference level corresponding to the case where there are no S-
 387 injectors in the chamber ($N_s = 0$). For a fixed value of N_s , \mathcal{A} configurations lead to a lower
 388 level of pressure fluctuations than C configurations. Instability frequencies are very close
 389 for C and \mathcal{L} configurations, although the amplitudes of pressure fluctuations are relatively
 390 different.

391

3.3. Effects of symmetry breaking on modal dynamics

392 This section is aimed at examining the consequences of symmetry breaking on the modal
 393 dynamics in the annular system. It is worth at this stage complementing the review of the
 394 literature by briefly examining articles that deal with azimuthal mode dynamics and more
 395 specifically with the switching taking place between spinning, standing and mixed modes
 396 (Krebs *et al.* (2002), Bourgouin *et al.* (2013), Worth & Dawson (2013), Worth & Dawson
 397 (2017), Prieur *et al.* (2017), Mazur *et al.* (2019)). It is also found that this switching prevails

12

Figure 7: Type \mathcal{L} (top) and type \mathcal{A} (bottom) configurations investigated.

398 in numerical simulations (Wolf *et al.* (2012)) and that the frequency of this phenomenon is
 399 relatively low compared to the acoustic frequency scale (Worth & Dawson (2017)).

400 These questions are actively investigated on the theoretical level, and models are developed
 401 to explain why some modes are preferred. Ghirardo & Juniper (2013) extended the model
 402 proposed by Noiray, Bothien & Schuermans (2011) by taking into account the effects of
 403 acoustic azimuthal velocity on the flames. Noiray & Schuermans (2013) showed that mode
 404 switching can be explained by introducing stochastic noise forcing in analytical models of
 405 annular systems. Another question of interest concerns the preferred location of the nodal line
 406 in rotationally symmetric annular combustors when the standing mode prevails. An attempt
 407 to explain these observations is made by considering spontaneous breaking of rotational
 408 and reflectional symmetries in the system (Indlekofer *et al.* (2022b)). Another theoretical
 409 description of the dynamics of azimuthal waves is proposed by Faure-Beaulieu & Noiray
 410 (2020) who show that the nature of the mode can be portrayed by making use of three slow-
 411 state variables, namely the amplitude, nature angle, and nodal line angle. Symmetry breaking
 412 in azimuthal combustion dynamics is also analyzed by Ghirardo *et al.* (2021) by making use
 413 of the method of averaging and considering small departures in the flame response gain with
 414 respect to baseline symmetric values.

415 Effects of symmetry breaking on modal dynamics in an annular system and on the nodal line
 416 position have been investigated in laboratory scale annular configurations. Experiments in
 417 the annular Rijke tube showed that the position of the nodal line coincides with the position of
 418 the heating grids with the lowest power for some staging patterns (Moeck, Paul & Paschereit
 419 (2010)). Dawson & Worth (2015) observed that placing baffles in the NTNU annular
 420 combustor chamber led to preferred standing modes whereas a configuration without baffles
 421 featured a permanent switching between standing and spinning modes. Symmetry breaking
 422 experiments in MICCA equipped with matrix burners showed that the orientation of the
 423 nodal line is controlled by the asymmetry pattern introduced in the system (Aguilar *et al.*
 424 (2021)).

425 It is also worth recalling that modal dynamics can be described using the spin ratio, s_r ,
 426 introduced by Bourgouin *et al.* (2013), which can be deduced from the wave amplitudes A_+
 427 and A_- :

$$428 \quad s_r = \frac{|A_+| - |A_-|}{|A_+| + |A_-|} \quad (3.1)$$

429 A pure standing mode corresponds to the case where $A_+ = A_-$, such that $s_r = 0$. For a spinning
 430 mode in the clockwise (respectively counterclockwise) direction, $A_- = 0$ (respectively

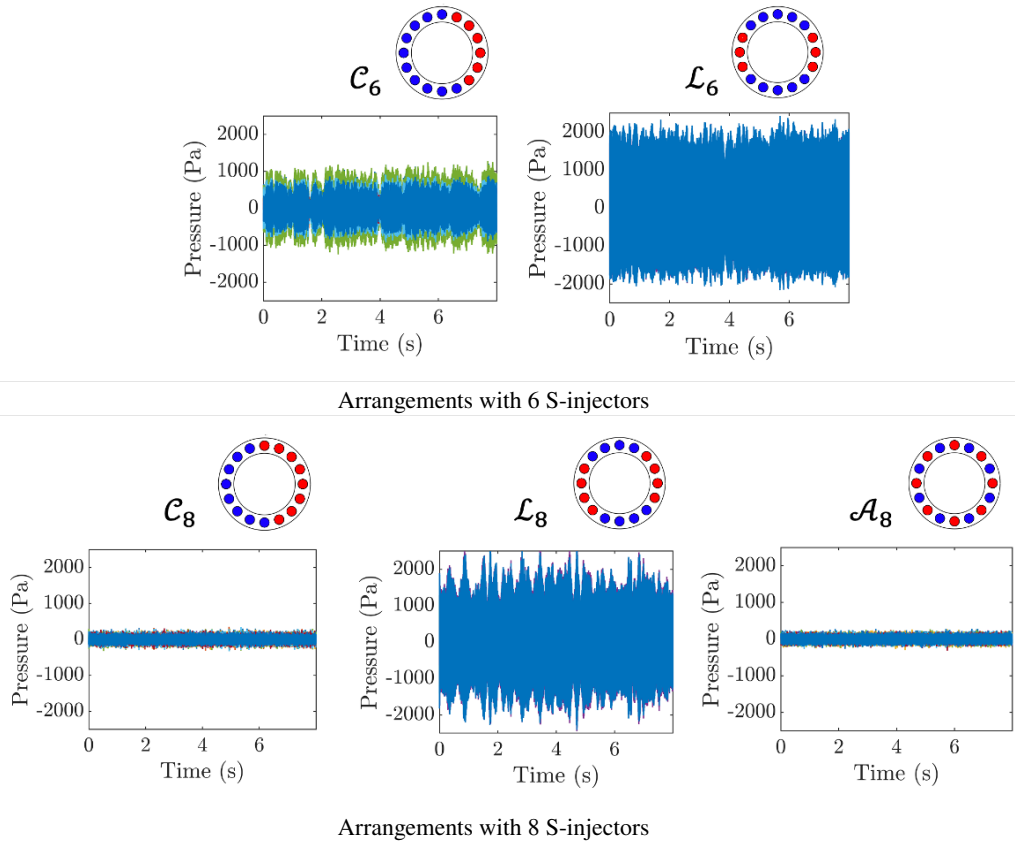


Figure 8: Pressure times series in the annular combustor MICCA-Spray for different configurations: C_6 and L_6 (top), and C_8 , L_8 , and A_8 (bottom). Experiments are carried out at an operating point of thermal power $\mathcal{P} = 118$ kW and an equivalence ratio $\phi = 0.9$.

431 $A_+ = 0$) and the corresponding spin ratios are $s_r = -1$ and $s_r = +1$ respectively. This spin
 432 ratio definition is close to that formulated by Evesque, Polifke & Pankiewitz (2003) based
 433 on acoustic energy considerations, but this earlier proposal does not distinguish clockwise
 434 and counterclockwise spinning motions. Another representation based on the quaternion
 435 variables (Ghirardo & Bothien (2018)) is also possible. It can be shown that the spin ratio
 436 is related to the “nature angle”, χ , by $s_r = \tan \chi$.

437 An interesting visualization of the modal characteristics consists in plotting the joint
 438 Probability Density Function $p(A_+, A_-)$ calculated over a time series of the pressure field in
 439 the annular system. This is exemplified in Figure 11 where this PDF is shown for different
 440 configurations of U and S injection units.

441 In these plots, the distinction between standing and spinning modes is that proposed by
 442 Worth & Dawson (2013):

- 443 • If $A_+/A_- < 1/2$ (i.e. $-1 < s_r < -1/3$), the mode is deemed as clockwise spinning.
- 444 • If $1/2 < A_+/A_- < 2$ (i.e. $-1/3 < s_r < 1/3$), the mode is deemed as standing.
- 445 • If $A_+/A_- > 2$ (i.e. $1/3 < s_r < 1$), the mode is deemed as counterclockwise spinning.

446 When there are no S-injectors in the system (configuration C_0), A_+ and A_- take a wide
 447 range of values, and a broad region of the $\{A_+, A_-\}$ plane is explored by the system: the
 448 mode switches from spinning to standing at a frequency of the order of a few Hz. When one

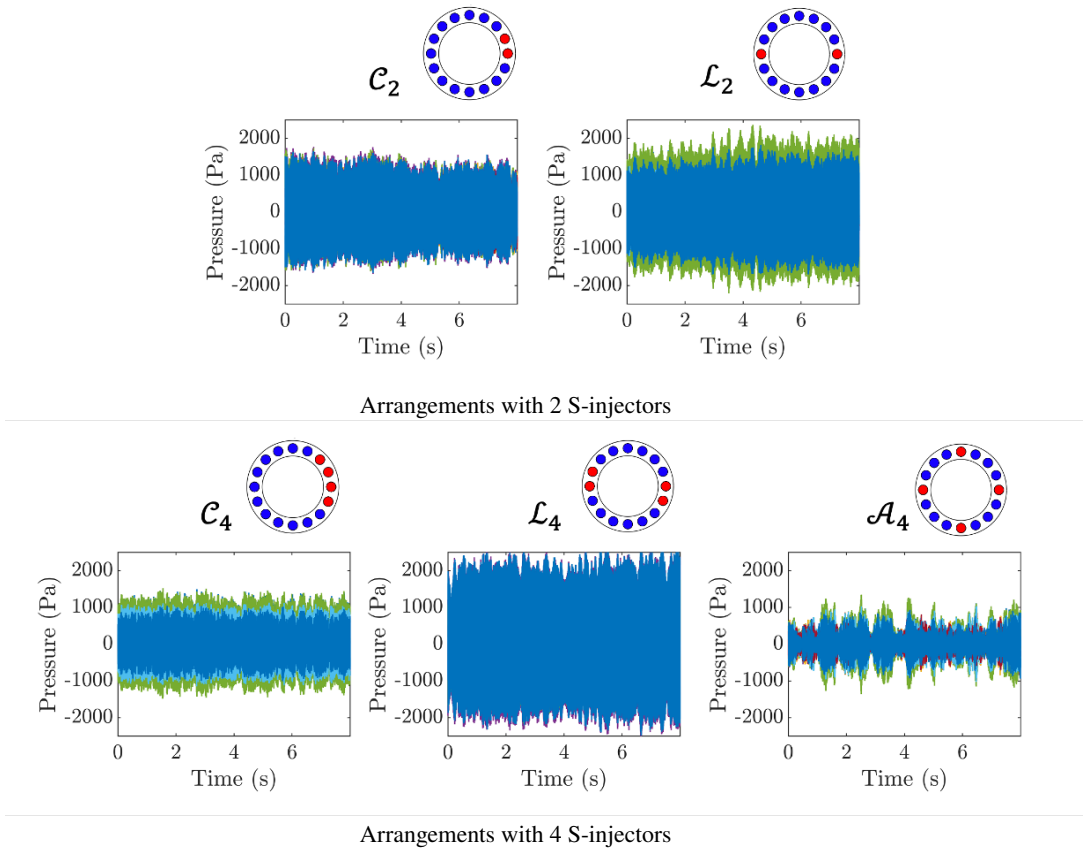


Figure 9: Pressure times series in the annular combustor MICCA-Spray for different configurations: C_2 and L_2 (top), and C_4 , L_4 , and A_4 (bottom). Experiments are carried out at an operating point of thermal power $\mathcal{P} = 118$ kW and an equivalence ratio $\phi = 0.9$.

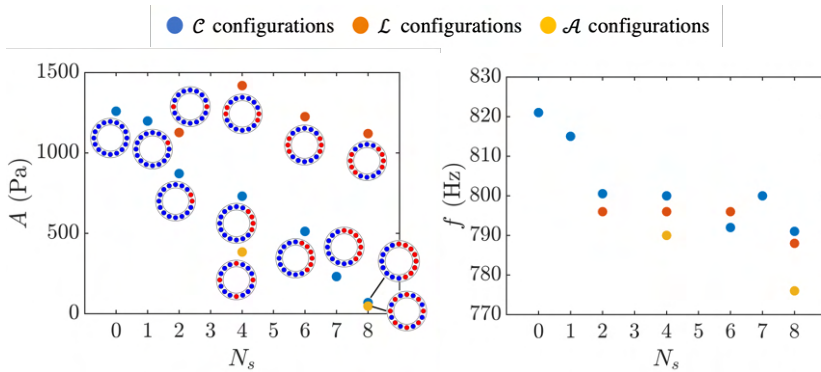


Figure 10: Instability amplitude (left) and frequency (right) as a function of the number of S injectors in MICCA-Spray, N_s , for different configurations: C (blue), L (orange), and A (yellow). Experiments are carried out at an operating point of thermal power $\mathcal{P} = 118$ kW and an equivalence ratio $\phi = 0.9$.

449 S injector is added (configuration C_1), a preferred spinning mode in the counterclockwise
450 direction is observed. When two or more S-injectors are present (configurations C_2 , C_4 , C_6 ,
451 \mathcal{L}_2 , \mathcal{L}_4 , \mathcal{L}_6 , and \mathcal{L}_8), a standing mode is preferred, as points of highest probability density
452 function value lie within the two dashed lines separating the standing mode from the spinning
453 modes.

454 The location of the S-injectors imposes the orientation of the nodal line, as can be seen
455 from the pressure recordings for configurations C_0 , C_8 , C_4 , and \mathcal{L}_4 presented in Fig. 12. For
456 configuration C_0 , which constitutes a reference unstable case, all the microphones record
457 similar levels of pressure fluctuations. For configurations C_4 and \mathcal{L}_4 , the positions where the
458 microphones recorded the lowest pressure fluctuations coincide with that of the S injectors.
459 Using these microphone recordings, the pressure field can be reconstructed using Eq. (2.4),
460 and the position of the nodal line (where the pressure fluctuations are the lowest) can be
461 determined.

462 Nodal line distributions are displayed in Fig. 13 for configurations C_2 , C_4 , \mathcal{L}_2 , and \mathcal{L}_4 .
463 They show narrower distributions for configurations C_4 and \mathcal{L}_4 than for C_2 and \mathcal{L}_2 . Another
464 way to analyze the nodal line position consists in representing the probability of the nodal line
465 location in the annular geometry, determined from the nodal line distribution, as illustrated in
466 Fig. 13 (bottom). For configuration C_2 , the nodal line passes through the S injectors, and for
467 configurations C_4 and \mathcal{L}_4 , the nodal line shows a preferred location between two injectors,
468 closer to an injector than to another neighbour of the same type. When there is a single S-
469 injector or when an odd number of S-injectors is in a C configuration, the nodal line passes,
470 respectively, through the unique injector or through the central unit in the C arrangement.
471 These findings generally correspond to what one might expect on a physical basis but it is
472 worth trying to explain what is observed by calculating the growth rates associated with the
473 different configurations and showing that the nodal line location is that corresponding to a
474 maximum in the growth rate (see section 4.3).

475 **4. Interpretation using acoustic energy balance equations and flame describing** 476 **functions**

477 It is now interesting to see if the previous experimental observations can be interpreted in a
478 unified framework. Results obtained suggest that it might be possible to derive a framework
479 that could suitably represent changes in the injection units by making use of the acoustic
480 energy balance applied to the annular geometry. This possibility will be explored in what
481 follows by making use of the assumption that the various injection units operate independently
482 from each other and that their flame describing functions may be assimilated to those
483 measured in the single sector experiments and displayed in section 2. This hypothesis is
484 validated by the results obtained by Patat *et al.* (2021) in a setup comprising a rectangular
485 combustion chamber equipped with injector units identical to those used in the present study.
486 The authors showed, by submitting an array of flames to transverse acoustic oscillations, that
487 the FDF of a flame placed at a pressure anti-nodal line is similar to the FDF of a flame at an
488 intermediate position between a pressure node and a pressure anti-node if they are submitted
489 to the same pressure oscillation at the outlet of the injector. The azimuthal flow modifies
490 the lateral dynamics but does not change the FDF, which essentially results from the axial
491 dynamics. The FDF measured in the single injector configuration SICCA-Spray can hence
492 be used to interpret the observations in MICCA-Spray. However, if the flames' spacing were
493 smaller, with strong interactions between the flames' fronts, this hypothesis might probably
494 not be valid anymore.

495 If one now considers that the flames formed by the various injectors operate independently
496 from each other it is possible to derive an expression of the source term based on the FDFs

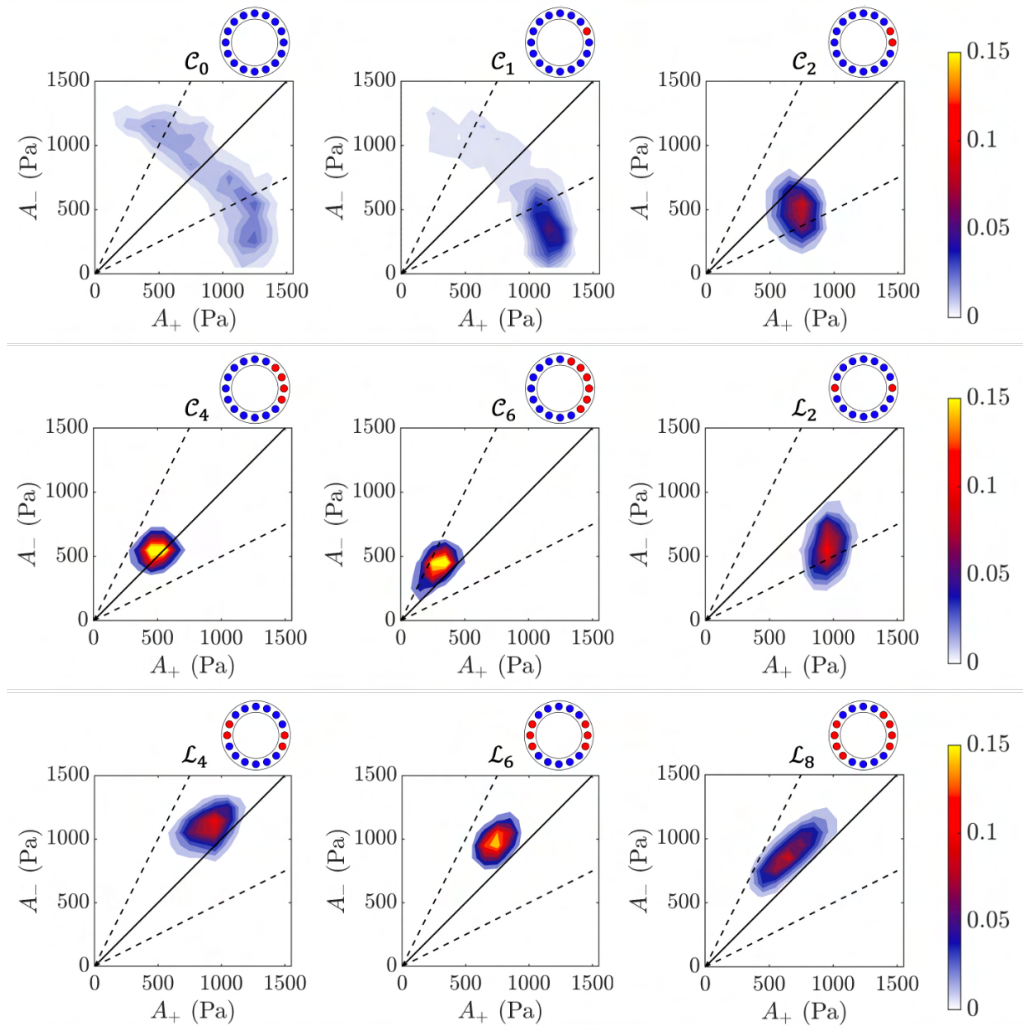


Figure 11: JPDF of A_+ and A_- determined from pressure time series. Top to bottom and left to right: C_0 , C_1 , C_2 , C_4 , C_6 , L_2 , L_4 , L_6 , and L_8 . Dashed lines, corresponding to $A_+/A_- = 1/2$ and $A_+/A_- = 2$, separate the standing mode from the spinning modes in the clockwise and counterclockwise directions.

497 of the flames formed by the two types of injectors. This will be a function of the number
 498 of injectors N_s and N_u and of their position in the annular system. This analysis will serve
 499 two purposes. First, obtain an estimate of the growth rate for the different configurations
 500 investigated. Knowing which configurations are stable and unstable will also enable to
 501 identify upper and lower bounds for the damping rate of the annular system. The second
 502 objective is to explain the nodal line locking in a preferred position observed for some
 503 configurations, by comparing the growth rates corresponding to different nodal line positions.

504

4.1. Acoustic energy balance framework

505 One seeks an analytical expression for the growth rate, as a function of the FDFs of the two
 506 types of injectors and their relative position in the annulus. The starting point of this analysis
 507 is the acoustic energy balance equation which reads

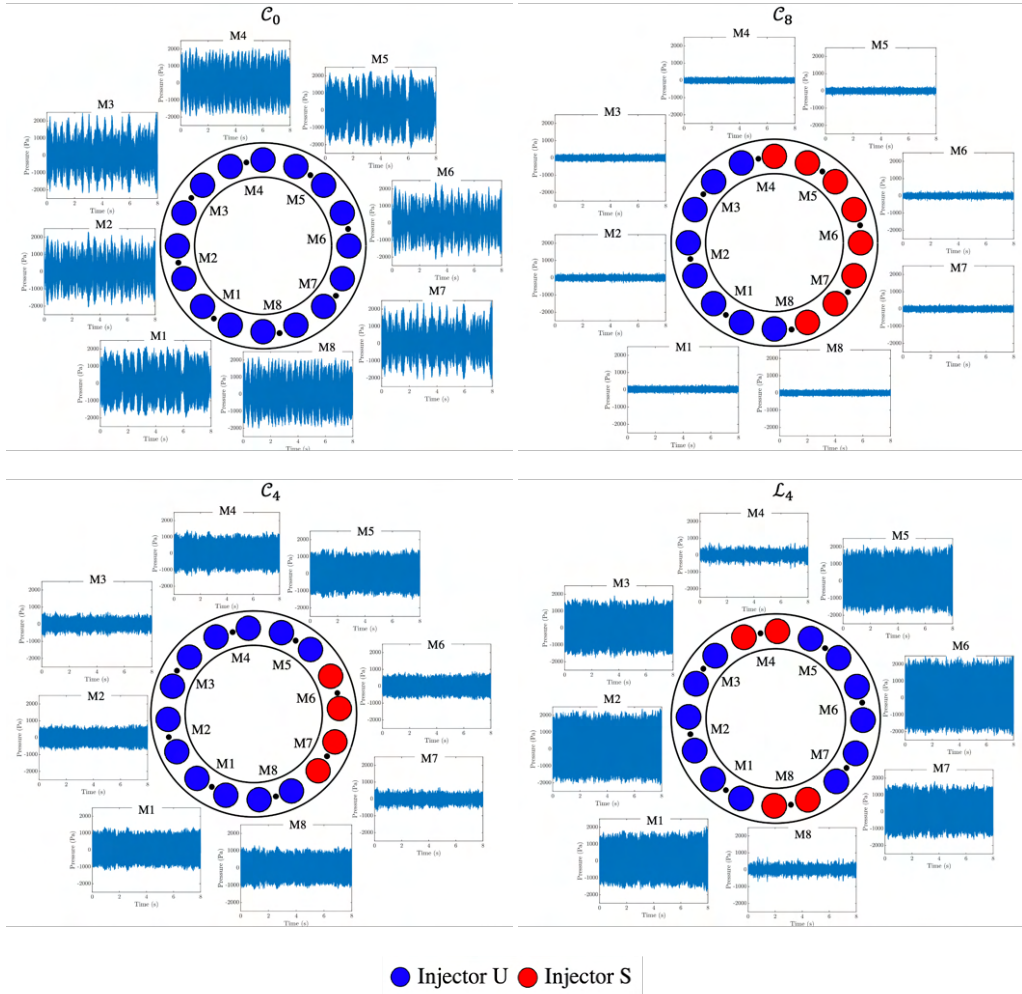


Figure 12: Pressure time series at different microphone positions for configurations C_0 (top left), C_8 (top right), C_4 (bottom left), and L_4 (bottom right).

$$508 \quad \frac{\partial \mathcal{E}}{\partial t} + \nabla \cdot \mathcal{F}_a = \mathcal{S} - \mathcal{D} \quad (4.1)$$

509 where \mathcal{E} , \mathcal{F}_a , \mathcal{S} , and \mathcal{D} are the instantaneous acoustic energy density, the acoustic energy
 510 flux, the Rayleigh source term, and the volumetric damping term respectively.

$$511 \quad \mathcal{E} = \frac{1}{2} \frac{p'^2}{\rho_0 c^2} + \frac{1}{2} \rho_0 v'^2 \quad (4.2)$$

$$512 \quad \mathcal{F}_a = p' \mathbf{v}' \quad (4.3)$$

$$513 \quad \mathcal{S} = \frac{\gamma - 1}{\rho_0 c^2} p' \dot{q}' \quad (4.4)$$

514 with p' , v' the acoustic pressure and velocity, \dot{q}' , the heat release rate fluctuations, ρ_0 , the
 515 ambient density, c , the speed of sound, and γ , the specific heat ratio.

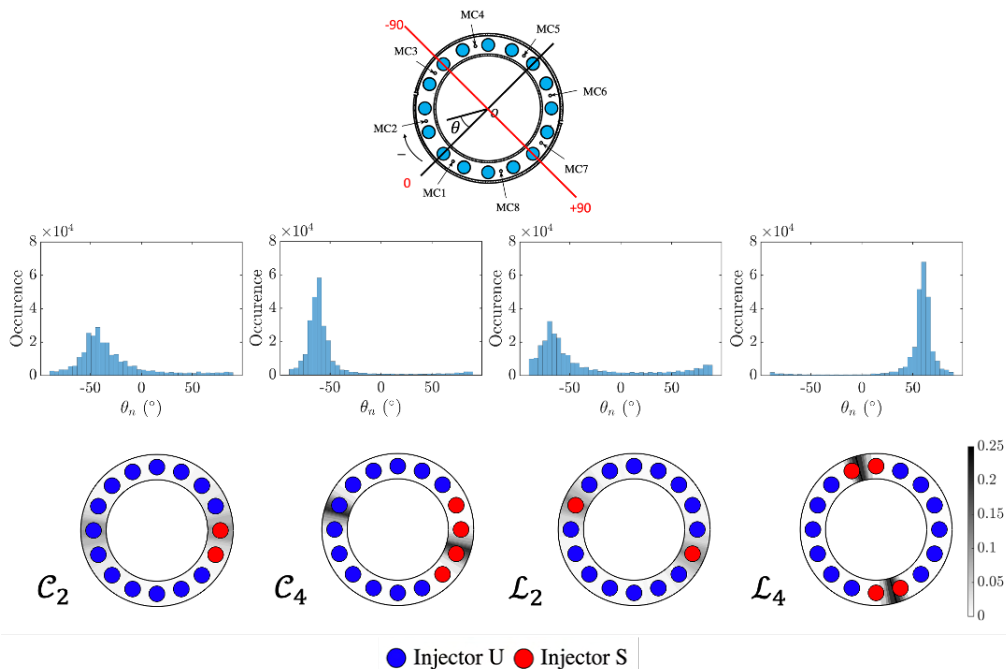


Figure 13: Top: origin and sign of the angles. Middle: nodal line distribution (with a bins' size of 4.5°) for configurations C_2 , C_4 , L_2 and L_4 (from left to right). Bottom: probability of the nodal line position.

516 In the case of harmonic oscillations, spatial and temporal variations may be decoupled,
 517 and one can write:

$$518 \quad p' = \text{Re}\{\tilde{p}(t)e^{-i\omega t}\}, v' = \text{Re}\{\tilde{v}(t)e^{-i\omega t}\}, q' = \text{Re}\{\tilde{q}(t)e^{-i\omega t}\} \quad (4.5)$$

519 where $\tilde{p}(t)$, $\tilde{v}(t)$, and $\tilde{q}(t)$ are slowly varying functions, and $\omega = 2\pi f$, with f the frequency
 520 of oscillation.

521 Integrating the balance equation over a period of oscillation yields an equation linking
 522 period averages

$$523 \quad \frac{\partial E}{\partial t} + \nabla \cdot \mathbf{F} = S - D \quad (4.6)$$

524 where E , \mathbf{F} , and S are the period averages of \mathcal{E} , \mathcal{F}_a , and \mathcal{S} . These quantities are conveniently
 525 determined with Eq. 4.7, valid if the slowly varying variables can be assumed constant over
 526 a cycle of oscillation:

$$527 \quad \frac{1}{T} \int_{[T]} a' b' dt = \frac{1}{2} \text{Re}\{\tilde{a}\tilde{b}^*\} \quad (4.7)$$

528 with $a' = \text{Re}\{\tilde{a}(t)e^{-i\omega t}\}$, $b' = \text{Re}\{\tilde{b}(t)e^{-i\omega t}\}$, and $*$ designating the complex conjugate.

529 One hence obtains

$$530 \quad E = \frac{1}{4} \frac{\widetilde{p\overline{p}}^*}{\rho_0 c^2} + \frac{1}{4} \rho_0 \overline{\mathbf{v}} \cdot \overline{\mathbf{v}}^* \quad (4.8)$$

$$531 \quad \mathbf{F} = \frac{1}{2} Re\{\widetilde{p\overline{\mathbf{v}}}\} \quad (4.9)$$

$$532 \quad S = \frac{\gamma - 1}{\rho_0 c^2} \frac{1}{2} Re\{\widetilde{p\overline{q}}\} \quad (4.10)$$

533 Taking the average of the balance equation over the volume V of the combustor, one gets:

$$534 \quad \frac{d\langle E \rangle}{dt} = \langle S \rangle - \langle D \rangle - \langle F \rangle \quad (4.11)$$

535 with $\langle E \rangle$, $\langle S \rangle$, and $\langle D \rangle$ the integrals over the volume V of E , S , and D , and $\langle F \rangle = \int_A \mathbf{F} \cdot \mathbf{n} dA$,
536 the surface integral of the normal energy flux.

537 Assuming that p' , v' , and q' have a common term $\exp(-i\omega t)$, with $\omega = \omega_r + i\omega'_i$ where
538 ω_r is the angular frequency and ω'_i represents the effective growth or decay rate of the
539 oscillations, one can divide Eq. 4.11 by $2\langle E \rangle$ to identify a growth rate ω_i and a damping rate
540 α

$$541 \quad \omega_i = \frac{1}{2\langle E \rangle} \langle S \rangle \quad (4.12)$$

$$542 \quad \alpha = \frac{1}{2\langle E \rangle} [\langle D \rangle + \langle F \rangle] \quad (4.13)$$

544 such that $\omega'_i = \omega_i - \alpha$ represents the effective growth rate, determining whether the oscillation
545 will grow or decay. ω_i represents the growth rate in the absence of damping and this term
546 can take positive or negative values. α is the damping rate, resulting from sources of acoustic
547 energy dissipation in the control volume and acoustic energy fluxes escaping the volume and
548 inducing a rate of change of the acoustic energy in the volume. Assuming that the boundaries
549 are only passive (that the acoustic flux leaving the volume is always positive or null), the
550 damping rate α is always positive and the oscillation will grow if $\omega_i > \alpha$.

551 To determine ω_i , one now has to calculate the period average of the Rayleigh source term

$$552 \quad \langle S \rangle = \frac{\gamma - 1}{\rho_0 c^2} \frac{1}{T} \int_{[T], V} p' q' dV dt \quad (4.14)$$

553 Introducing the volume integrated heat release rate fluctuations $\dot{Q} = \int_V q' dV$, and assuming
554 that the pressure is constant in the region where there are heat release rate fluctuations, i.e.
555 that the flames are compact with respect to the acoustic wavelength, one gets:

$$556 \quad \langle S \rangle = \dot{Q}_0 \frac{\gamma - 1}{\gamma} \frac{1}{T} \int_{[T]} \frac{p'}{p_0} \frac{\dot{Q}'}{\dot{Q}_0} dt \quad (4.15)$$

557 which can be rewritten as:

$$558 \quad \langle S \rangle = \dot{Q}_0 \frac{\gamma - 1}{\gamma} \frac{1}{2} Re\left\{ \frac{\widetilde{p}}{p_0} \left[\frac{\widetilde{\dot{Q}'}}{\dot{Q}_0} \right]^* \right\} \quad (4.16)$$

559 One now seeks an analytical expression for the relative heat release rate fluctuations.
560 Introducing the flame describing function, \mathcal{F} , linking relative heat release rate fluctuations
561 to relative velocity fluctuations,

$$562 \quad \mathcal{F} = \frac{\widetilde{\dot{Q}'}/\dot{Q}_0}{\widetilde{\mathbf{v}}/\overline{\mathbf{v}}} \quad (4.17)$$

20

563 and using the effective impedance, ζ , to link relative velocity fluctuations to relative pressure
564 fluctuations at the flame position, one gets

$$565 \quad \frac{\widetilde{\dot{Q}}'}{\dot{Q}_0} = \mathcal{F} \frac{1}{\bar{v}} \frac{\widetilde{p}}{\rho_0 c \zeta} = \frac{\mathcal{F}}{\zeta} \frac{1}{\gamma M} \frac{\widetilde{p}}{p_0} \quad (4.18)$$

566 where M is the Mach number of the flow at the flame.

567 Introducing $\mathcal{F} = G_F e^{i\varphi_F}$ and $\zeta = G_\zeta e^{i\varphi_\zeta}$, one can write the relative heat release rate
568 fluctuations in the following form

$$569 \quad \frac{\widetilde{\dot{Q}}'}{\dot{Q}_0} = \frac{G_F}{G_\zeta} \frac{1}{\gamma M} \frac{\widetilde{p}}{p_0} e^{i\varphi_F - i\varphi_\zeta} \quad (4.19)$$

570 In the case of an annular combustor, assuming that the 1A1L mode is involved in the
571 coupling and considering a mixed azimuthal structure, pressure fluctuations can be cast in
572 the form:

$$573 \quad \widetilde{p}(x, \theta) = [a e^{i\theta - i\omega t} + b e^{-i\theta - i\omega t}] \psi(x) \quad (4.20)$$

574 To simplify notations, the complex amplitudes A_+ and A_- of Eq. 2.4 have been replaced by a
575 and b . As already indicated in section 2, Eq. 4.20 constitutes an approximate representation
576 of the pressure field that neglects distortions induced by circumferential staging in the 1A
577 azimuthal modal structure.

578 The axial wavefunction corresponding to the 1L mode is $\psi(x) = \cos[\pi x/2l]$. It is assumed
579 that the flames are compact with respect to the acoustic wavelength and one may neglect any
580 variation in the axial direction and assume that the axial wavefunction takes a constant value
581 at the flame position, $\psi(x) \simeq \psi(x_f)$, and simply designate this value by ψ_f .

582 The volume integrated period average contribution of the j -th flame, located at an
583 azimuthal angle θ_j , to the source term using Eq. 4.16 writes:

$$584 \quad \langle S_j \rangle = \frac{1}{2} \frac{(\gamma - 1)}{\gamma} \dot{Q}_0 \frac{1}{\gamma p_0^2} \frac{1}{M} \frac{G_F}{G_\zeta} \psi_f^2 \text{Re}(J) \quad (4.21)$$

585 where

$$586 \quad J = (a e^{i\theta} + b e^{-i\theta})(a^* e^{-i\theta} + b^* e^{i\theta}) e^{-i(\varphi_j - \varphi_\zeta)} \quad (4.22)$$

587 Rewriting

$$588 \quad a = |a| e^{i\Phi_+}, \quad b = |b| e^{i\Phi_-} \quad (4.23)$$

589 and introducing

$$590 \quad \theta_0 = (\Phi_- - \Phi_+)/2 \quad (4.24)$$

591 which corresponds to the ‘‘spatial phase’’ term determining the pressure antinode location in
592 the quaternion representation (Ghirardo & Bothien (2018)). This is easily verified for example
593 in the case of a standing mode by taking $|a| = |b|$. One obtains after a few calculations:

$$594 \quad \langle S_j \rangle = \frac{1}{2} \frac{(\gamma - 1)}{\gamma} \dot{Q}_0 \frac{1}{\gamma p_0^2} \frac{1}{M} \frac{G_F}{G_\zeta} \psi_f^2 \cos(\varphi_j - \varphi_\zeta) [|a|^2 + |b|^2 + 2|a||b| \cos(2(\theta - \theta_0))] \quad (4.25)$$

595 Now the acoustic energy integrated over a period and the combustor volume reads

$$596 \quad \langle E \rangle = \int_V \left[\frac{1}{4} \frac{\widetilde{p} \widetilde{p}^*}{\rho_0 c^2} + \frac{1}{4} \rho_0 \widetilde{\mathbf{v}} \cdot \widetilde{\mathbf{v}}^* \right] dV \quad (4.26)$$

597 Which can be simplified into

$$598 \quad \langle E \rangle = \frac{1}{4} \frac{1}{\rho_0 c^2} [|a|^2 + |b|^2] V \quad (4.27)$$

599 Using the growth rate expression (4.12) and making use of the assumption that the different
600 injectors operate independently from each other, one may write

$$601 \quad \omega_i = \frac{1}{2\langle E \rangle} \sum_{j=1}^N \langle S_j \rangle \quad (4.28)$$

602 which yields after insertion of (4.25) and (4.27):

$$603 \quad \omega_i = \frac{(\gamma - 1)}{\gamma} \frac{\dot{Q}_0}{p_0 V} \psi_f^2 \sum_{j=1}^N \frac{G_{Fj}}{M G_{\zeta j}} \cos(\varphi_{Fj} - \varphi_{\zeta j}) \left[1 + \frac{2|a||b|}{|a|^2 + |b|^2} \cos(2(\theta_j - \theta_0)) \right] \quad (4.29)$$

604 The growth rate appears like a weighted sum of the contributions of the individual flames
605 depending on the position of the injectors with respect to the pressure anti-nodal line position
606 (θ_0), appearing in the $\cos(2(\theta_j - \theta_0))$ term. It also depends on the phase difference between
607 the flame describing functions and the phase of the specific impedance that links the pressure
608 and velocity disturbances acting on the flame through ($\cos(\varphi_{Fj} - \varphi_{\zeta j})$), and on the gain of
609 the FDFs of the various types of injectors.

610 It is first interesting to consider a case where all injectors have the same FDF and impedance
611 gain and phase values, i.e. when $G_{Fj} = G_F$, $\varphi_{Fj} = \varphi_F$, $G_{\zeta j} = G_\zeta$, and $\varphi_{\zeta j} = \varphi_\zeta$. In that
612 case, one finds that the second term in the brackets in expression (4.29) does not contribute
613 to the sum over the N injectors and one obtains:

$$614 \quad \omega_i = \frac{(\gamma - 1)}{\gamma} \frac{N \dot{Q}_0}{p_0 V} \psi_f^2 \frac{G_F}{M G_\zeta} \cos(\varphi_F - \varphi_\zeta) \quad (4.30)$$

615 In this particular case of identical flame responses for all the injectors, one finds that the
616 growth rate does not depend on the nature of the mode that assures the coupling, and that ω_i
617 is the same for mixed, CCW or CW spinning, and standing modes. This definitely explains
618 experimental observations where these various modes appear and continuously switch
619 between the various possible amplitudes of the CCW and CW composing the azimuthal
620 structure. This ceases to be true when injectors feature different responses characterized by
621 differences in the gains G_F and phases φ_F .

622 It is also interesting to consider two limiting cases corresponding to a standing mode and
623 a pure spinning mode. In the first case, $|a| = |b|$, and Eq. (4.29) becomes:

$$624 \quad \omega_i = 2(\gamma - 1) \frac{\dot{Q}_0}{\gamma p_0 V} \psi_f^2 \sum_{j=1}^N \frac{G_{Fj}}{M G_{\zeta j}} \cos(\varphi_{Fj} - \varphi_{\zeta j}) \cos^2(\theta_j - \theta_0) \quad (4.31)$$

625 In the latter expression, the $G_{Fj} \cos(\varphi_{Fj} - \varphi_{\zeta j})$ term associated with each flame is
626 weighted by the $\cos^2(\theta_j - \theta_0)$ term, depending on the position of the flame with respect to
627 the anti-nodal line.

628 In the second case, one of the wave amplitudes a or b vanishes and the growth rate takes
629 the form:

$$630 \quad \omega_i = (\gamma - 1) \frac{\dot{Q}_0}{\gamma p_0 V} \psi_f^2 \sum_{j=1}^N \frac{G_{Fj}}{M G_{\zeta j}} \cos(\varphi_{Fj} - \varphi_{\zeta j}) \quad (4.32)$$

22

631 If the mode is spinning, the contribution of each flame to the total growth rate is independent
632 of its position in the annular system.

633 4.2. Validation of the analytical framework

634 The objective of the present section is to validate the analytical framework with two test cases
635 before using it to determine the growth rates for all the configurations investigated. To do so,
636 it is convenient to work with the dimensionless quantity $\langle S_j \rangle / \dot{Q}_0$, the source term at flame j
637 divided by the mean heat release rate in one flame, since it can be determined experimentally
638 from simultaneous pressure and photomultiplier recordings using Eq. (4.15) recalled below:

$$639 \quad \langle S_j \rangle / \dot{Q}_0 = \frac{\gamma - 1}{\gamma} \frac{1}{T} \int_{[T]} \frac{p'_j}{p_0} \frac{\dot{Q}'}{\dot{Q}_0} dt \quad (4.33)$$

640 The flames behaving in a quasi-premixed fashion (see section 2.2), the relative heat
641 release rate fluctuations can be approximated by the relative intensity fluctuations recorded
642 by a photomultiplier equipped with a OH* filter, $I'/I \approx \dot{Q}'/\dot{Q}_0$.

643 The source term at the j -th flame can also be determined analytically and expressed as a
644 function of the level of peak pressure fluctuations in the chamber at injector j , $|p'_j/p_0|^2$, by
645 combining Eqs. (4.16) and (4.19):

$$646 \quad \langle S_j \rangle / \dot{Q}_0 = \frac{1}{2} \frac{\gamma - 1}{\gamma^2} \frac{G_{Fj}}{G_{\zeta j}} \frac{1}{M} \left| \frac{p'_j}{p_0} \right|^2 \cos(\varphi_{Fj} - \varphi_{\zeta j}) \quad (4.34)$$

647 The level of peak pressure fluctuations at injector j , $|p'_j/p_0|^2$, constitutes a data input from
648 experiments for this validation case.

649 The experimental setup used for this study is presented in Fig. 14 (first column). Eight
650 photomultipliers are used to record the relative light intensity fluctuations emitted by eight
651 adjacent flames on one half of the annulus. Pressure fluctuations are reconstructed at each
652 injector position using pressure recordings and Eq. (2.4). The values of $\langle S_j \rangle / \dot{Q}_0$ thus obtained
653 experimentally and analytically for eight flames will be compared for two configurations
654 leading to a well-defined standing mode with the nodal line location controlled by the
655 position of S injectors: \mathcal{L}_4 and a variation of configuration \mathcal{L}_4 , denoted \mathcal{L}_{4+1} , in which an
656 additional S injector was placed close to the pressure antinode.

657 The different quantities appearing in the source term expression and the methodology used
658 to determine them are gathered in Tab. 2. The gain and phase values of the FDF are obtained
659 from FDF measurements presented in section 2.2. FDF gain and phase are evaluated at the
660 frequency $f_{11} = 808$ Hz, corresponding to the eigenvalue of the 1AIL mode of the MICCA-
661 Spray combustion chamber (Eq. (2.3)). The impedance phase φ_{ζ} and the product MG_{ζ} are
662 determined with the procedure described in Appendix B. It is also shown that the impedances
663 ζ_U and ζ_S of the different injection units are quite close. Although the respective pressure
664 drop values of injectors U and S are different, their transfer matrices (discussed in Appendix
665 B) are mainly determined by the air distributor and terminal plate, which are common to the
666 two types of injectors, the swirler only having a minor influence on the coefficients of these
667 matrices. As a consequence, $\zeta_S \approx \zeta_U$, and one may use the same effective impedance ζ .

668 The comparison between experimental data and the analytical determination of the source
669 term is presented in Fig. 14 (third column). Experimental measurements for the source term
670 show that the flames located at the pressure node do not contribute significantly to the total
671 source term. The flames bringing the highest contribution are those located at the pressure
672 antinode. Placing a S injector close to the pressure antinode (configuration \mathcal{L}_{4+1} , Fig. 14,
673 bottom) induces a drop in the source term value at the position of the S injector facing

Parameter	Determination procedure
N	Number of injectors in the annular system (here $N = 16$).
θ_j	Location of the j -th injector: $\theta_j = (j - 1)2\pi/N$.
θ_0	Pressure anti-nodal line location.
V	Volume of the annular chamber $V = \mathcal{P}_a l_a l$, with \mathcal{P}_a , the annulus mean perimeter, l_a , the annulus width, and l , the quartz walls length.
\dot{Q}_0	Mean heat release rate in one flame.
ψ_f	Value of the axial eigenfunction determined at x_f : $\psi = \psi_1(x_f) = \cos(\pi x_f/(2l))$.
G_{Fj}, φ_{Fj}	Gain and phase of the FDF determined at the frequency of the 1A1L mode, f_{11} : $G_{Fj} = G_{Fj}(f_{11})$, $\varphi_{Fj} = \varphi_{Fj}(f_{11})$.
φ_ζ	Phase of the specific impedance at the flame determined with the method described in Appendix B.
MG_ζ	Product of the Mach number at the flame (M) by the specific impedance gain (G_ζ) determined with the method described in Appendix B.
$ p'_j/p_0 ^2$	Level of peak pressure fluctuations at injector j , determined from measurements with the microphones flush-mounted on the backplane of the chamber.
p_0	Ambient pressure, 10^5 Pa.
γ	Specific heat ratio, $\gamma = 1.4$.

Table 2: Parameters used for the growth rate calculations and procedure used to determine these quantities.

674 photomultiplier “PM4”. This can be linked to the smaller FDF gain value measured for
675 injector S, compared to that for injector U. A good qualitative and quantitative agreement
676 between the experimental measurements and the evaluation of the analytical expression
677 is found. The drop in the value of the source term observed for configuration \mathcal{L}_{4+1} at the
678 position of the S-injector facing photomultiplier “PM4” is also well retrieved by the analytical
679 expression of the source term.

680

4.3. Nodal line locking

681 The analytical expression of the growth rate is now used to interpret mode selection and
682 nodal line locking phenomena.

683 At this point, it is first useful to recall theoretical results on how breaking the symmetry in
684 an annular system changes the associated eigenvalues and modal structures. A perfectly
685 symmetric annular combustor features degenerate eigenvalues. In this case, the mode
686 structure is spinning, standing, or of mixed type. Symmetry breaking induced by the staging of
687 different injectors (or the introduction of Helmholtz resonators) splits the initially degenerate
688 eigenvalue into a couple of distinct eigenvalues, characterized by different frequencies and
689 growth rates (Stow & Dowling (2003); Bauerheim *et al.* (2014); Bauerheim, Cazalens &
690 Poinso (2015)). It is found by Bauerheim *et al.* (2014) that staging two types of injectors in
691 an annular system gives rise to standing modes with perpendicular nodal lines and introduces
692 a “splitting strength”, controlling the difference between the eigenfrequencies and growth
693 rates associated with the two modes. The latter quantity depends on the flame dynamical
694 characteristics and the staging pattern.

695 One may now interpret the experimental results obtained in MICCA-Spray in the light of
696 these theoretical findings in combination with the analysis of the growth rate expressions for
697 the different configurations. To that end, Fig. 15 shows the growth rate as a function of the

24

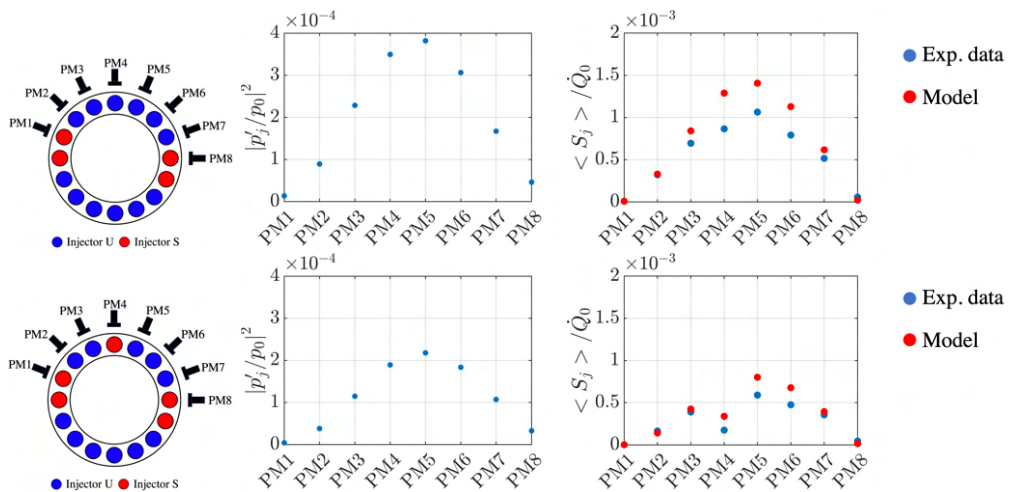


Figure 14: Experimental validation of the analytical framework: configurations \mathcal{L}_4 (top) and \mathcal{L}_{4+1} (bottom). Left: experimental setup, with the positions of the U and S injectors and the photomultipliers. Center: peak pressure fluctuations $|p'_j/p_0|^2$ at the eight photomultiplier locations. Right: comparison between $\langle S_j \rangle / \dot{Q}_0$ determined experimentally (blue) and analytically (red) at the eight photomultiplier positions.

698 nodal line location for all the configurations investigated. Power spectral densities (PSD) of
 699 the pressure signals, together with nodal line angular positions and spin ratio time series are
 700 also reported for unstable configurations in Appendix C to support the analysis carried out
 701 in this section.

702 Let us start with configurations C_0 and C_{16} , where all the injectors are of one type.
 703 Theoretically, the mode is degenerate. The power spectral densities of the pressure signals
 704 feature a single peak and mixed modes are observed experimentally with the nodal line
 705 position sweeping a broad range of locations (see Appendix C). The associated growth rate
 706 given by Eq. (4.31) shows no dependence on the nodal line position, which is coherent with
 707 the experimental observations. For case C_8 , the growth rate shows no variations with the
 708 nodal line location θ_n either and its value is half way between those found for C_0 and C_{16}
 709 and probably lower than the damping rate since this case is found to be stable in the tests.

710 For configuration C_1 where a S injector replaces a U injector, the mode is of mixed type
 711 and a single frequency peak is observed in the power spectral density (see the corresponding
 712 plots reported in Appendix C). The mathematical evaluation of Eq. (4.31) indicates a small
 713 difference between the minimum and maximum values of the growth rate. One may infer
 714 that, for this staging pattern, the splitting strength is low, giving rise to a small loss of
 715 degeneracy, with a frequency difference between the two eigenmodes below the frequency
 716 resolution of the PSD ($\Delta f = 4$ Hz). In addition, the beating observed in the pressure signal
 717 at a frequency around 2 Hz, displayed in Appendix C, is another indication of this slight loss
 718 of degeneracy. It is also interesting to note that, in this particular configuration, the mixed
 719 modal structures are preferentially of the CCW spinning wave type. One might think that this
 720 preferred spinning direction could be linked to the tangential flow induced by the injection
 721 unit swirlers which are all oriented in the same direction. However, this global rotating flow
 722 is slow (Durox *et al.* (2015)) and rotates in the CW direction. The statistical preference
 723 observed for the CCW mode in configuration C_1 is probably not linked to the bulk swirl, as
 724 already discussed in Rajendram Soundararajan *et al.* (2022a).

725 For alternate configurations \mathcal{A}_4 and \mathcal{A}_8 , the growth rate ω_i is independent of the nodal

726 line location and the mode is degenerate, as a result of the remaining discrete rotational
 727 symmetry. Arrangement \mathcal{A}_8 leads to stable operation and the oscillations in configuration
 728 \mathcal{A}_4 correspond to mixed modes at a reduced amplitude level (see Appendix C).

729 Eq. (4.31) highlights interesting features for configurations $C_2, C_4, C_6, \mathcal{L}_2, \mathcal{L}_4, \mathcal{L}_6,$ and
 730 \mathcal{L}_8 . Theoretically, these configurations, for which the splitting strength is expected to take
 731 high values, present two distinct eigenvalues associated to two different growth rates and
 732 eigenfrequencies. The two resulting modes are standing and the associated nodal lines are
 733 perpendicular. Depending on the growth rate values, one mode can prevail and be effectively
 734 observed in practice. Power spectral densities of the pressure signals for these cases, reported
 735 in Appendix C, feature a single well-defined peak. A standing mode with a fixed nodal line is
 736 observed and the other analytically possible mode, with a nodal line perpendicular to the first
 737 mode, is not observed experimentally. Examining the mathematical properties of Eq. (4.31),
 738 two extrema appear for two perpendicular nodal line positions (it is worth stressing at this
 739 point that, in Fig. 15, although only two possible standing modes are predicted theoretically
 740 for these cases, the growth rate ω_i is evaluated for a range of nodal line positions θ_n to examine
 741 the change in shape of the function for these different staging patterns). For configurations
 742 $C_2, C_4,$ and $C_6,$ Eq. (4.31) indicates that the nodal line leading to a maximum of the growth
 743 rate passes at equal distances from the S-injectors which is consistent with the experimental
 744 observations. For type \mathcal{L} configurations, the corresponding nodal lines are aligned with the
 745 diameter joining the centres of the two groups of S-injectors placed on opposite sides of the
 746 annular chamber. Hence, of the two possible nodal line orientations for these non-degenerate
 747 cases, the nodal line leading to a maximum growth rate is selected and indeed observed
 748 experimentally. To finish, the difference between the maximum and minimum value of the
 749 growth rate increases with the number of S injectors for these cases and this can be interpreted
 750 as reflecting an increase in the value of the splitting strength.

751 4.4. Growth rate calculations and estimation of the damping rate

752 It is now instructive to consider the growth rates associated to different configurations and use
 753 their values to derive an estimate of the damping rate corresponding to instabilities coupled
 754 by the 1A1L mode.

755 The damping rate α plays a key role in thermo-acoustic analysis but its value is generally
 756 not measured or quoted. A theoretical estimate is difficult to obtain because the processes
 757 that give rise to damping are not always easy to model. One possibility consists in using
 758 resonance techniques and measuring the quality factor of the system under stable operation.
 759 This only gives an effective damping rate α' that needs to be corrected for the flame influence
 760 (Paliès *et al.* (2011)). A second approach relies on system identification methods applied to
 761 simultaneous recordings of pressure and heat release rate fluctuations (Boujo *et al.* (2016)).
 762 A third possibility consists in estimating the Rayleigh source term under self-sustained
 763 oscillations at a limit cycle (Durox *et al.* (2009), Vignat (2020)). Starting from Eq. (4.11),

$$764 \quad \frac{d\langle E \rangle}{dt} = \langle S \rangle - \langle D \rangle - \int_A \mathbf{F} \cdot \mathbf{n} dA \quad (4.35)$$

765 and assuming steady self-sustained oscillations, the $d\langle E \rangle/dt$ term vanishes, and one gets:

$$766 \quad \langle D \rangle + \int_A \mathbf{F} \cdot \mathbf{n} dA = \langle S \rangle \quad (4.36)$$

767 Hence, under steady self-sustained oscillations, the source term is in equilibrium with the
 768 acoustic losses, which result from damping and outgoing acoustic energy fluxes. The source
 769 term $\langle S \rangle$ was evaluated by Durox *et al.* (2009) and Vignat (2020) through simultaneous

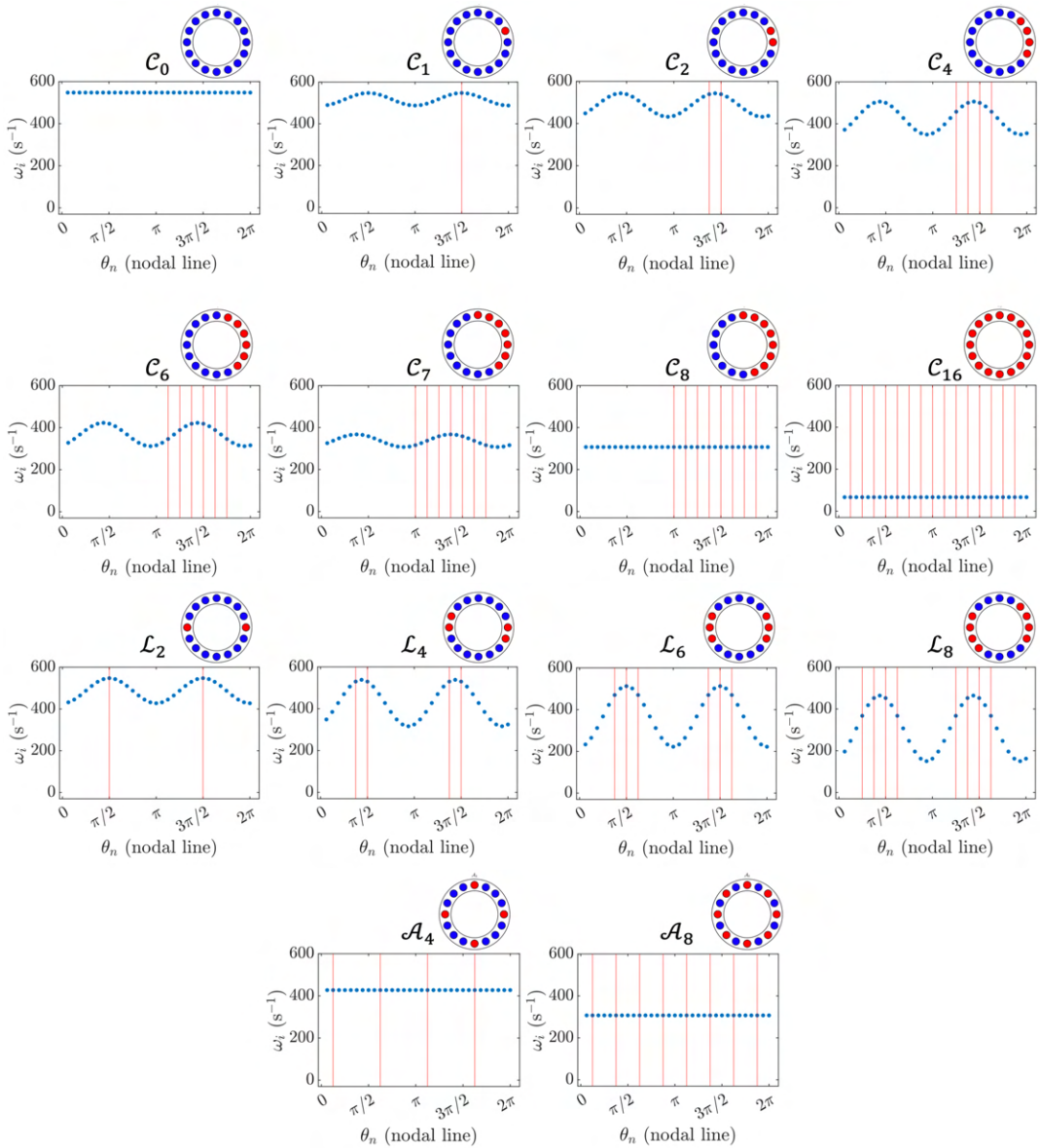


Figure 15: Growth rate as a function of the nodal line position θ_n for all the configurations investigated. Red vertical lines correspond to the position of S-injectors in the annular system. Although only two possible standing modes with perpendicular nodal line positions are theoretically predicted for cases C_2 , C_4 , C_6 , L_2 , L_4 , L_6 , and L_8 , the growth rate ω_i is evaluated for a range of nodal line positions θ_n to examine the change in shape of the function for these different staging patterns.

770 photomultipliers and microphone recordings. It is shown by Vignat (2020) that the latter
 771 method and the approach based on system identification proposed by Boujo *et al.* (2016)
 772 yield comparable results in the case of instabilities coupled by a purely axial mode.

773 In this section, growth rates ω_i are calculated using the analytical framework presented in
 774 section 4.1 for configurations C_0 , C_2 , C_4 , C_6 , C_7 , and C_8 , and then for L_2 , L_4 , L_6 , L_8 , L_{10} ,
 775 and L_{12} , and finally for A_4 and A_8 . These results are then used to estimate the damping

776 rate. For a given configuration, the growth rate can be determined for any combination of $|a|$
 777 and $|b|$ and one can then see which combination provides the highest growth rate. In many
 778 situations, equal values of these amplitudes ($|a| = |b|$) yield the maximum value. This is
 779 consistent with the experimental observations, as these configurations give rise to standing
 780 modes. Eq. (4.29) with $|a| = |b|$ will hence be used to determine the growth rates. The nodal
 781 line location is the one leading to the maximum value of the growth rate.

782 It is worth recalling that the growth rates obtained with the analytical expression are
 783 determined for low levels of modulation amplitude, since FDF data is only available for
 784 levels of relative velocity fluctuations around 10% in the frequency range of interest (around
 785 800 Hz). They hence correspond to linear growth rates. The values of the growth rate will
 786 change with the level of modulation amplitude, $\omega_i = \omega_i(v' = 0)g(v'/\bar{v})$, where g can be
 787 increasing or decreasing for intermediate values of v'/\bar{v} and then becomes a decreasing
 788 function of v'/\bar{v} at high amplitude levels.

789 Figure 16 shows the evolution of the growth rate as a function of the number of S-injectors
 790 for C , \mathcal{L} , and \mathcal{A} configurations. For the three types of configurations investigated, the
 791 calculated growth rate decreases with the number of S-injectors in the system, and for a fixed
 792 number of S-injectors, growth rates for type C and \mathcal{A} staging patterns are lower than those
 793 found for \mathcal{L} arrangements.

794 The calculated values of the growth rates enable to get an estimate of the damping rate
 795 of the system: stable and unstable points enable to identify upper and lower bounds of the
 796 damping rate. If a point is unstable, its growth rate is higher than the damping rate of the
 797 system. If a point is stable, its growth rate is lower than the damping rate of the system. Hence,
 798 the unstable point with the lowest growth rate constitutes the upper limit of the damping rate,
 799 and the stable point with the highest growth rate, the lower limit. In order to distinguish
 800 between stable and unstable points, the two criteria defined in Latour *et al.* (2023) will be
 801 used:

- 802 • The root mean square (rms) pressure is at least 3 times higher than a baseline level
 803 corresponding to the rms pressure level of noise under combustion and flow, measured for a
 804 stable operating point, which is typically 80 Pa.
- 805 • The power spectral density exhibits a peak, $SPL_{\Delta f}^m$, that exceeds the maximum level
 806 measured in the baseline configuration, $SPL_{\Delta f}^{bl,m}$, by at least 25 dB: $SPL_{\Delta f}^m \geq SPL_{\Delta f}^{bl,m} + \Delta S$
 807 (with $\Delta S = 25$ dB). This condition ensures that the signal is dominated by a well-defined
 808 frequency tone.

809 The upper and lower limits thus determined correspond to the grey band plotted in Fig. 16,
 810 left. Configuration C_7 , which is marginally unstable (the criterion for the rms pressure level
 811 is fulfilled, but not that for the power spectral density peak), is inside the grey band. One finds
 812 that the damping rate is between 310 and 390 s^{-1} . This value is consistent with that found
 813 by Vignat (2020), through source term evaluation from simultaneous photomultiplier and
 814 pressure measurements during self-sustained oscillations coupled by a longitudinal mode in
 815 the annular combustor MICCA-Spray.

816 One may ask whether the limit cycle amplitude can be linked in some way to the effective
 817 growth rate calculated in the linear range. Intuitively, one expects that high values of this
 818 rate will lead to high levels of oscillation. This possible link is examined in Fig. 16 (right)
 819 where the instability amplitude A is plotted as a function of the effective growth rate $\omega'_i =$
 820 $\omega_i - \alpha$, determined analytically from lower and upper estimates of α (310 and 390 s^{-1} ,
 821 corresponding to the grey band in Fig. 16 (left)). One can see that configurations associated
 822 to high positive values of the effective growth rate correspond to high levels of limit cycle
 823 instability amplitude. Configurations associated to negative values of the effective growth
 824 rate correspond to stable operation in MICCA-Spray. It is also interesting to point out that

28

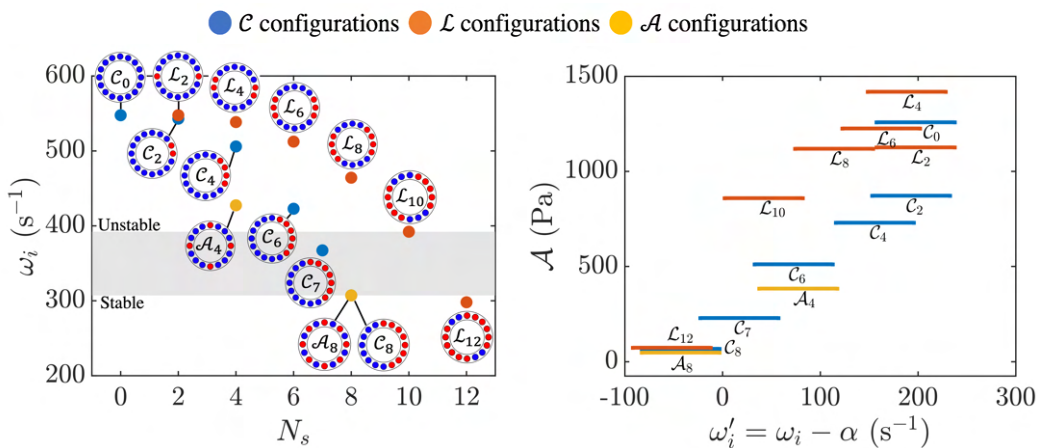


Figure 16: Growth rates determined with the analytical model (left) and experimental instability amplitudes \mathcal{A} as a function of the effective growth rate $\omega'_i = \omega_i - \alpha$ (right) for configurations $\mathcal{C}_0, \mathcal{C}_2, \mathcal{C}_4, \mathcal{C}_6, \mathcal{C}_7,$ and \mathcal{C}_8 (blue), $\mathcal{L}_2, \mathcal{L}_4, \mathcal{L}_6, \mathcal{L}_8, \mathcal{L}_{10},$ and \mathcal{L}_{12} (orange), and \mathcal{A}_4 and \mathcal{A}_8 (yellow). The grey band appearing in the left subfigure separates stable points from unstable points, providing an indication for the lower and upper values of the damping rate.

825 for similar values of the growth rate, the level of pressure oscillations at limit cycle also
 826 depends on the type of configuration (\mathcal{C} , \mathcal{L} , or \mathcal{A}). This may be due to the fact that gain
 827 saturation (reflected by the g function in the expression $\omega_i = \omega_i(v' = 0)g(v'/\bar{v})$) depends
 828 on the configuration or that the damping rate changes with the configuration.

829 5. Conclusions

830 Different circumferential staging configurations are investigated experimentally in the
 831 laboratory-scale annular combustor MICCA-Spray by mixing two types of injectors,
 832 designated by U and S, featuring significantly different flame responses and correspondingly
 833 different flame describing functions. When all injectors are of the U-type, the system
 834 exhibits strong combustion instabilities coupled by the 1A1L mode and the azimuthal
 835 structure involves variable proportions of clockwise and counterclockwise waves. The nature
 836 of the mode is in that case of mixed type, with no preferred location for the pressure nodal
 837 line. When all injectors are of S-type, the regime of operation is stable. It is found that
 838 azimuthal arrangements in which the two types of injectors U and S are mixed, notably
 839 influence the amplitude of oscillation and affect the modal nature. The changes in dynamics
 840 depend on the number and relative position of S-injectors. In a configuration where injectors
 841 of the same family are side by side, one observes that the oscillation amplitude is diminished
 842 as the number of S-injectors is augmented. When the S-injectors form two groups that are
 843 diametrically opposed, it is found that the coupling takes place through a standing 1A1L
 844 mode with a nodal line that is aligned with the median diameter connecting the two groups of
 845 S-injectors. Alternate configurations \mathcal{A} involving 4 or 8 S-injectors are shown to efficiently
 846 reduce the pressure oscillations in the annular system. An analytical framework relying on
 847 the acoustic energy balance equation is used to derive estimates of the growth rate, as a
 848 function of the injectors flame describing functions and of their circumferential location
 849 in the annular combustor. This general expression is used to explain many of the features
 850 observed experimentally. According to this expression, the growth rates corresponding to
 851 the spinning, mixed and standing modes are identically equal, when all the injectors are of

852 the same type. It is next shown that when nodal line locking occurs for certain configurations
 853 of the S-injectors, the nodal line azimuthal orientation corresponds to a position that is
 854 such that the growth rate reaches its highest possible value. Another outcome of these
 855 experiments, in combination with the growth rate values, is the possibility to obtain an
 856 estimate of the damping rate for instabilities coupled by the 1AIL mode. In terms of
 857 practical implications, these findings indicate that azimuthal staging may be used to damp
 858 thermo-acoustic instabilities but that the position of the injectors has to be carefully chosen
 859 since some arrangements damp the instability, this is the case of “side-by-side” arrangements
 860 or type \mathcal{A} configurations, while others, in which the S-units occupy the two ends of a
 861 diameter, are much less effective or even lead to enhanced amplitudes of oscillation. Finally,
 862 the theoretical growth rate expressions derived in this article have more general value in that
 863 they give access to the stability rating of geometrically simple annular combustion systems.

864 **Acknowledgements.** The authors wish to thank Dr. Yoann Méry from Safran Aircraft Engines for suggesting
 865 to analyze the impact of azimuthal staging on the occurrence and level of instabilities. [The authors also wish](#)
 866 [to thank the reviewers for their comments and suggestions.](#)

867 **Funding.** This work is partially supported as part of France 2030 programme “ANR-22-CE05-0022-02”
 868 FlySAFe project.

869 **Declaration of interests.** The authors report no conflict of interest.

870 **Appendix A: Effect of head loss differences on the equivalence ratio**

871 The pressure loss in an injection unit is typically expressed in terms of a bulk velocity U_b
 872 and a head loss coefficient as $\Delta p = \sigma(1/2)\rho U_b^2$. In the MICCA-Spray annular combustor, all
 873 the injectors have the same plenum for the air intake, and the common fuel rail is pressurized
 874 at a high level, allowing a constant fuel flow rate in each injector. Let us consider a system
 875 with n_1 injectors of type 1 and n_2 injectors of type 2, with respective head loss coefficients
 876 σ_1 and σ_2 . The bulk velocities in these two types of injectors are denoted U_1 and U_2 . In
 877 what follows, one seeks to quantify the effects of the difference in head loss coefficient on
 878 the equivalence ratios at the different injectors.

879 The pressure loss through the two types of injectors must be the same so that

$$880 \quad \Delta p = \sigma_1(1/2)\rho U_1^2 = \sigma_2(1/2)\rho U_2^2 \quad (5.1)$$

881 This defines the ratio of the bulk velocities through the two types of units

$$882 \quad \frac{U_1}{U_2} = \left(\frac{\sigma_2}{\sigma_1}\right)^{1/2} \quad (5.2)$$

883 Now, consider the total mass flow rate \dot{m} in the system. If the head loss coefficients are all
 884 equal, the flow velocities in each injectors are also equal

$$885 \quad \dot{m} = n\rho AU \quad (5.3)$$

886 If one now considers n_1 injectors of type 1 and n_2 injectors of 2, the total mass flow rate
 887 becomes

$$888 \quad \dot{m} = n_1\rho AU_1 + n_2\rho AU_2 \quad (5.4)$$

889 And replacing the left hand side term by the expression in Eq. (5.3), one has

$$890 \quad n\rho AU = n_1\rho AU_1 + n_2\rho AU_2 \quad (5.5)$$

n_S	1	2	3	4	5	6	7	8
$(\delta\phi/\phi)_U$	0.02	0.03	0.04	0.06	0.07	0.08	0.10	0.11
$(\delta\phi/\phi)_S$	-0.22	-0.20	-0.19	-0.17	-0.15	-0.14	-0.12	-0.11
ϕ_U	0.91	0.93	0.94	0.95	0.96	0.97	0.99	1.0
ϕ_S	0.70	0.72	0.73	0.75	0.76	0.78	0.79	0.80

Table 3: Effects of different numbers of S injection units on the equivalence ratios of the U and S units.

891 and then using Eq. (5.1), one finally obtains

$$892 \quad U = \frac{n_1}{n} \left(\frac{\sigma_2}{\sigma_1} \right)^{1/2} U_2 + \frac{n_2}{n} U_2 \quad (5.6)$$

893 Thus the velocities through injectors 1 and 2 read

$$894 \quad U_2 = U \frac{1}{1 + \frac{n_1}{n} \left[\left(\frac{\sigma_2}{\sigma_1} \right)^{1/2} - 1 \right]}, \quad U_1 = U \frac{\left(\frac{\sigma_2}{\sigma_1} \right)^{1/2}}{1 + \frac{n_1}{n} \left[\left(\frac{\sigma_2}{\sigma_1} \right)^{1/2} - 1 \right]} \quad (5.7)$$

895 The relative differences in velocities in injectors 1 and 2 compared to the case where all
896 the injectors are the same are

$$897 \quad \frac{(U_2 - U)}{U} = \frac{-\frac{n_1}{n} \left[\left(\frac{\sigma_2}{\sigma_1} \right)^{1/2} - 1 \right]}{1 + \frac{n_1}{n} \left[\left(\frac{\sigma_2}{\sigma_1} \right)^{1/2} - 1 \right]}, \quad \frac{(U_1 - U)}{U} = \frac{\frac{n_2}{n} \left[\left(\frac{\sigma_2}{\sigma_1} \right)^{1/2} - 1 \right]}{1 + \frac{n_1}{n} \left[\left(\frac{\sigma_2}{\sigma_1} \right)^{1/2} - 1 \right]} \quad (5.8)$$

898 The last two expressions indicate that, if $\sigma_2 > \sigma_1$ then $U_2 < U$ and $U_1 > U$ and may now
899 be used to quantify the impact in terms of global equivalence ratio. This quantity measures
900 the mixture ratio with respect to its value under stoichiometric conditions:

$$901 \quad \phi = \frac{\dot{m}_f / \dot{m}_a}{(\dot{m}_f / \dot{m}_a)_{st}} \quad (5.9)$$

902 Since the mass flow rate of fuel is the same in all injectors, relative equivalence ratio
903 perturbations resulting from the bulk velocity variations read

$$904 \quad \frac{\delta\phi}{\phi} = -\frac{\delta\dot{m}_a}{\dot{m}_a} = -\frac{\delta U}{U} \quad (5.10)$$

905 Noting that injectors U and S are such that $\sigma_U > \sigma_S$, one immediately deduces that the
906 operating point is shifted towards higher values of equivalence ratio for injectors U and
907 towards lower values for injectors S. Table 3 gathers the equivalence ratio variations for
908 different numbers of injectors S in the system.

909 One now seeks to quantify the effects of these equivalence ratio shifts on the dynamics
910 of the flames formed by injectors U and S. When MICCA-Spray is equipped with $N = 16$
911 identical injectors, at the operating point chosen for this study, the global equivalence ratio
912 is $\phi = 0.9$ and the thermal power, $\mathcal{P}_{MICCA} = 118$ kW. FDFs were thus measured in SICCA-
913 Spray for injectors S and U, at a fixed thermal power $\mathcal{P}_{SICCA} = \mathcal{P}_{MICCA}/N = 7.4$ kW,
914 but for different equivalence ratios ($\phi = 0.8, 0.85$, and 0.9 for injector S and $\phi = 0.9, 0.95$,
915 and 1.0 for injector U), to determine the effects of differences in equivalence ratio on flame
916 dynamics. Measurements for equivalence ratios below $\phi = 0.8$ are not available because
917 these operating points exceed the limits of the mass flow rate controllers.

918 The measured FDFs, plotted in Fig. 17, only feature slight differences between the nominal

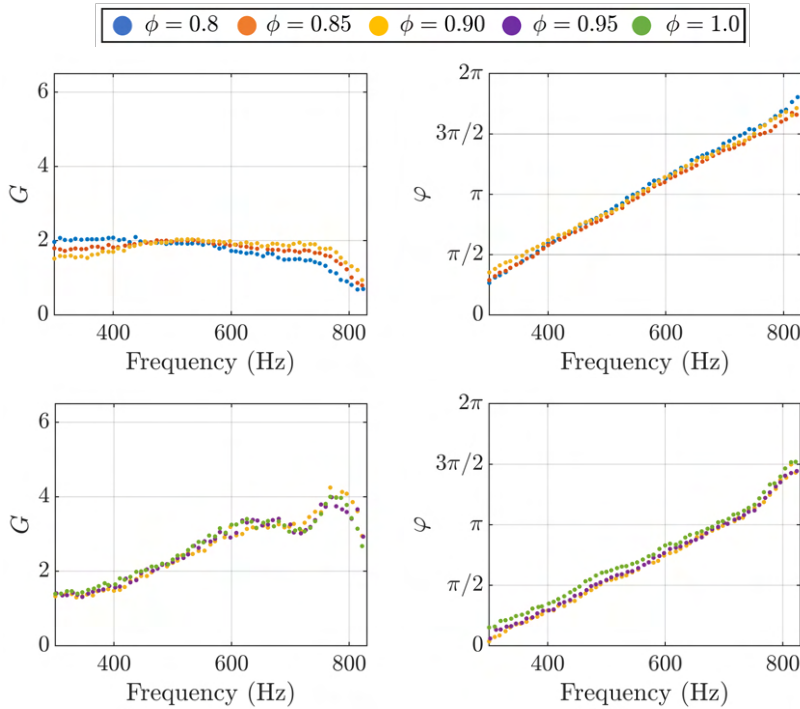


Figure 17: Effects of equivalence ratio on FDF gain (left) and phase (right). Measurements were carried out in SICCA-Spray at a thermal power $\mathcal{P}_{SICCA} = 7.4$ kW. Only the curves corresponding to the lowest level of modulation amplitude are represented. Top: injector S ($\phi = 0.8, 0.85, \text{ and } 0.9$). Bottom: injector U ($\phi = 0.9, 0.95, \text{ and } 1.0$).

919 gain and phase curves obtained at $\phi = 0.9$ and those corresponding to the S-injector operating
 920 at $\phi = 0.8$ or 0.85 . Similar observations also hold for injector U in the interval of equivalence
 921 ratios covered in the present experiments (from 0.9 to 1.0). Hence, the equivalence ratio
 922 variations resulting from the mixing of the different types of injectors only have a weak
 923 impact on the dynamics of the individual flames.

924 Appendix B: Determination of the effective impedance ζ

925 To evaluate the growth rate (Eq. 4.29), one has to determine the effective impedance ζ that
 926 connects the pressure field to the velocity disturbances acting on the upstream side of the
 927 flame.

928 This impedance is here determined experimentally from the simultaneous recording
 929 of pressure and heat release fluctuations in a single experiment in which MICCA-Spray
 930 features self-sustained oscillations. A “pressure-based” describing function, \mathcal{F}_p , connecting
 931 the relative pressure and relative heat release rate fluctuations can be determined from these
 932 measurements for different flames in the annular combustor:

$$933 \quad \mathcal{F}_p = \frac{\widetilde{\dot{Q}'}/\dot{Q}_0}{\widetilde{p}/p_0} \quad (5.1)$$

934 where, $\widetilde{\dot{Q}'}/\dot{Q}_0$ and \widetilde{p}/p_0 correspond, respectively, to the relative heat release rate and pressure
 935 fluctuations, and $p_0 = 10^5$ Pa is a reference pressure.

32

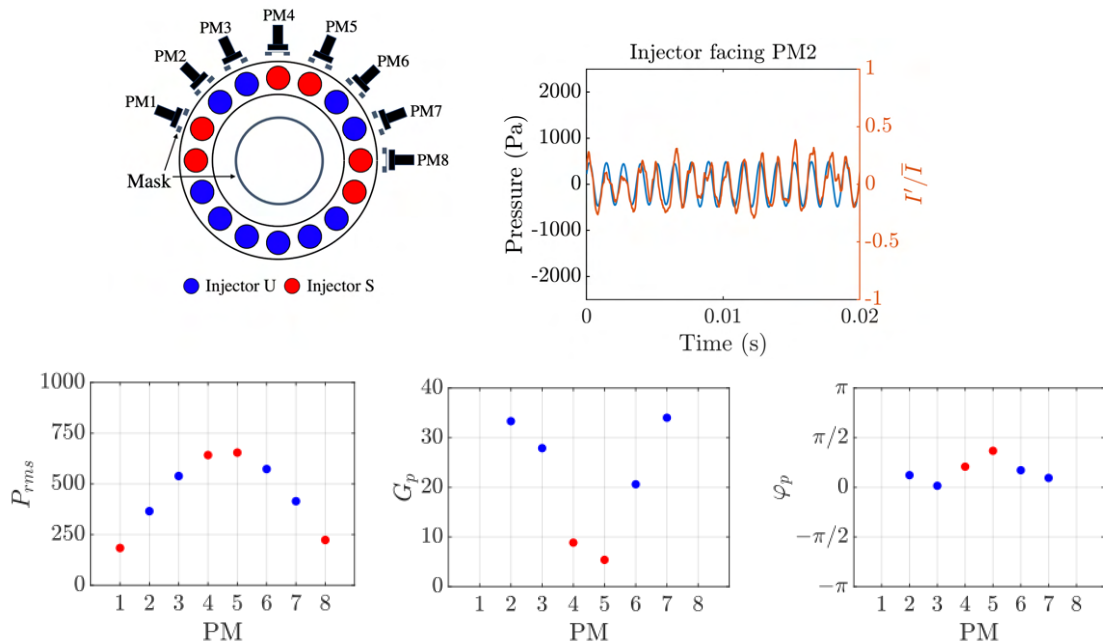


Figure 18: Top left: the MICCA-Spray setup in configuration \mathcal{L}_{4+2} for simultaneous photomultipliers (PM) and pressure recordings. Top right: Simultaneous pressure and PM recordings at the injector facing PM2, used for the determination of MG_ζ and φ_ζ (“calibration injector”). Bottom row: pressure root mean square at the injectors facing PM1 to PM8 (left), pressure-based FDF gain (center) and phase (right) at the injectors facing PM1 to PM8.

936 One can then link the pressure-based FDF to the FDF, \mathcal{F} , and the impedance ζ using Eq.
 937 (4.18):

$$938 \quad \mathcal{F}_p = \frac{\mathcal{F}}{\zeta} \frac{1}{\gamma M} \quad (5.2)$$

939 Finally, introducing $\mathcal{F}_p = G_p e^{i\varphi_p}$, one can express MG_ζ and φ_ζ as a function of the
 940 pressure-based FDF and FDF gain and phase values, G_F and φ_F :

$$941 \quad MG_\zeta = \frac{G_F}{G_p} \frac{1}{\gamma}, \quad \varphi_\zeta = \varphi_F - \varphi_p \quad (5.3)$$

942 The FDF data being only available for small values of the relative velocity fluctuations,
 943 it is therefore necessary to use an experiment in which the level of oscillation is low and
 944 corresponds to the range that is covered by the available FDF data set. This condition can be
 945 fulfilled by suitably choosing a configuration that leads to a low amplitude limit cycle.

946 The injectors arrangement (labelled “ \mathcal{L}_{4+2} ” and shown in Fig. 18, corresponding to
 947 configuration \mathcal{L}_4 to which two adjacent S injectors are placed at the pressure anti-node) and
 948 the flame location in the annular system to be used for the determination of the impedance
 949 is chosen to ensure that pressure fluctuations levels are low or moderate so that the level of
 950 fluctuation is compatible with the available FDF data. Eight photomultipliers equipped with
 951 a 10 nm bandpass filter centered at 310 nm record the light intensity emitted by OH* for
 952 eight adjacent flames located on one half of the annulus. The experimental setup, with the

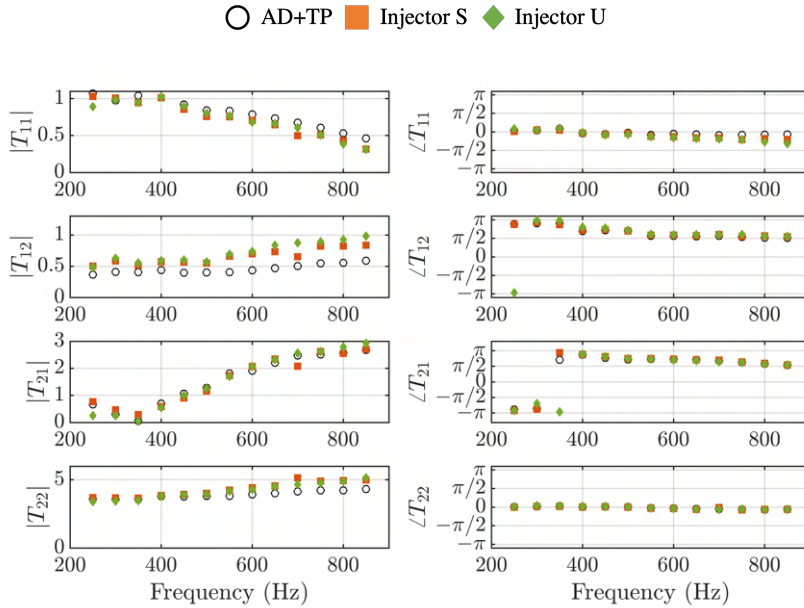


Figure 19: Transfer matrices of injectors U and S, and the injector without swirler, “AD+TP” (for “Air Distributor-Terminal Plate”), determined experimentally using the two-load method. The measurements were carried out in presence of a bias flow and the resulting velocity at the injector outlet is $U_b = 12 \text{ m}\cdot\text{s}^{-1}$.

953 photomultipliers and microphones position, is displayed in Fig. 18. A mask, placed in front of
 954 each photomultiplier acts as a spatial filter so that each sensor only records the light emitted
 955 by one flame. Another cylindrical mask, placed inside the inner cylindrical quartz, hides the
 956 flames in the background. For configuration \mathcal{L}_{4+2} , the mode is standing, and the measured
 957 root mean square pressure is reported for the injectors facing the eight photomultipliers in
 958 Fig. 18, bottom left.

959 The gain and phase values of the obtained pressure-based FDFs are shown in Fig. 18. Only
 960 points presenting a coherence between the pressure and heat release rate signal above 0.9
 961 are retained in this dataset (flames facing PM2 to PM7, the data corresponding to the flames
 962 facing PM1 and PM8 was removed). The flame used for the determination of MG_ζ is that
 963 facing PM2, designated as “calibration injector” in Fig. 18, since in this position, the flame is
 964 submitted to a moderate level of pressure fluctuations and the signal-to-noise ratio remains
 965 good (see the pressure and PM recordings at the injector facing PM2 presented in Fig. 18,
 966 top right).

967 For the determination of MG_ζ and φ_ζ using Eq. (5.3), G_F and φ_F were evaluated at
 968 the instability frequency for configuration \mathcal{L}_{4+2} , $f = 800 \text{ Hz}$. Additional experiments
 969 were carried out in SICCA-Spray to link velocity fluctuations to pressure fluctuations,
 970 to ensure that the range of pressure fluctuations for the FDF data is compatible with the level
 971 of pressure fluctuations measured in MICCA-Spray at the measurement point. One finally
 972 obtains $\varphi_\zeta = 1.2\pi$ and $MG_\zeta = 0.09$. These values are then used in the calculations in
 973 sections 4.2 and 4.3, for all the arrangements investigated.

974 It is next shown that the impedance ζ can be assumed to be the same for the two
 975 types of injectors U and S. This assumption is supported by the transfer matrices obtained
 976 experimentally for injectors U and S using the two-load method (Munjaj & Doige (1990)).
 977 These matrices are displayed in Fig. 19. The transfer matrix coefficients for the injector

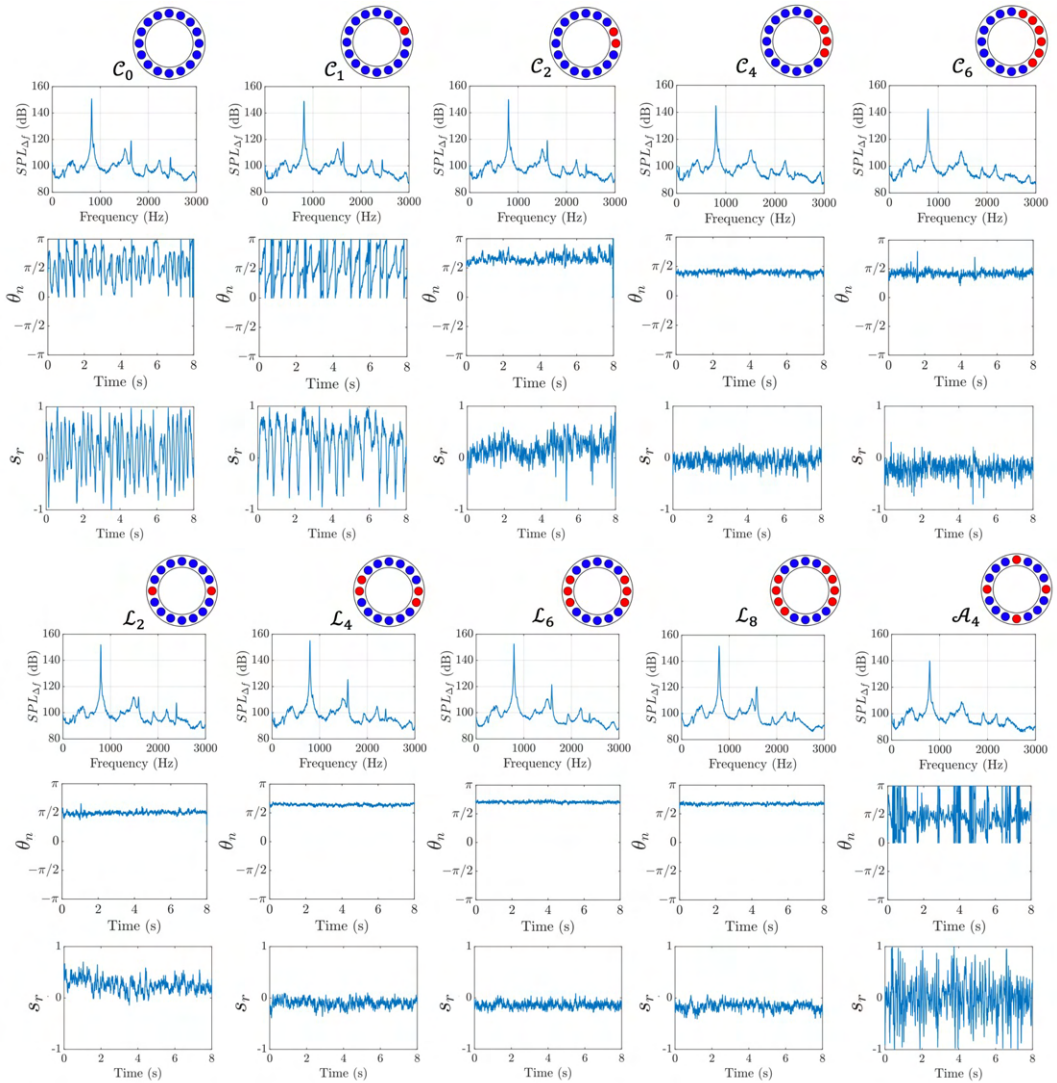


Figure 20: Pressure signal power spectral densities, spin ratio (s_r) and nodal line (θ_n) time series for configurations C_0 , C_1 , C_2 , C_4 , C_6 , L_2 , L_4 , L_6 , and A_4 . The origin and sign of the angles for the nodal line time-series are defined in Fig. 13.

978 without swirler, “AD+TP” (Air Distributor-Terminal Plate) are also reported in Fig. 19 to
 979 determine the effect of the swirler on the transfer matrix of the injection units. Further details
 980 on the measurements can be found in Latour *et al.* (2023b). Although these two injectors
 981 feature different pressure drop values, experimental results show that their transfer matrices
 982 are very close, and mainly determined by the air distributor and terminal plate, the swirler
 983 only having a small influence on the coefficients. Hence, the impedance can be considered
 984 to be the same for injectors U and S, $\zeta_S = \zeta_U$. One may then infer that the differences in
 985 flame dynamics observed between injectors S and U have their origin in differences in flame
 986 structures and their response to incident disturbances rather than in changes in the acoustic
 987 impedance at the flame.

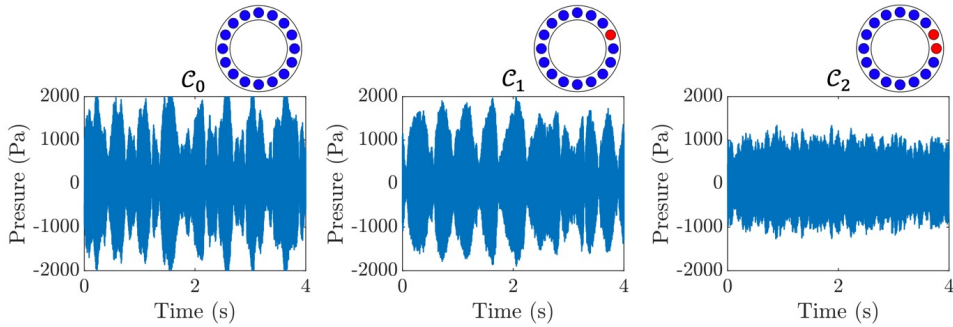


Figure 21: Pressure time series for configurations C_0 , C_1 , and C_2 showing a beating behaviour for arrangements C_0 and C_1 .

988 Appendix C: Degenerate and non-degenerate mode features

989 The pressure signal power spectral densities (PSD) along with the spin ratio and the nodal
 990 line time series are displayed in Fig. 20 for configurations C_0 , C_1 , C_2 , C_4 , C_6 , \mathcal{L}_2 , \mathcal{L}_4 , \mathcal{L}_6 , \mathcal{L}_8 ,
 991 and \mathcal{A}_4 to complete the modal analysis of Sec. 4.3. The origin and sign of the angles for the
 992 nodal line time series are defined in Fig. 13.

993 A single peak appears in the PSD of the pressure signal for these unstable configurations,
 994 indicating that, for the non-degenerate modes associated to staging patterns for which the
 995 splitting strength is expected to take high values (C_2 , C_4 , C_6 , \mathcal{L}_2 , \mathcal{L}_4 , \mathcal{L}_6 , and \mathcal{L}_8), only one
 996 mode, shown to correspond to the maximum value of the growth rate (see Sec. 4.3), is
 997 observed in practice.

998 The PSD for arrangement C_1 features a single peak, but the associated pressure recordings
 999 exhibit a beating oscillation (see Fig. 21, where the pressure time series for configurations
 1000 C_0 , C_1 , and C_2 reported), hinting that the splitting strength induced by symmetry breaking
 1001 only leads to a small frequency difference between the two modes (smaller than the frequency
 1002 resolution of the spectrum which is $\Delta f = 4$ Hz). This beating disappears in configuration C_2 .

1003 To finish, the mode is expected to remain degenerate for case C_0 , and the power spectral
 1004 densities of the pressure recordings feature a single peak. However, a beating behaviour is
 1005 observed in the pressure signal (see Fig. 21, left), which may possibly be linked to the slight
 1006 break in symmetry due to the bulk swirling flow induced in the annular system, as discussed
 1007 by Bauerheim, Cazalens & Poinso (2015). This hypothesis may be verified by estimating the
 1008 frequency split resulting from the presence of a tangential mean flow in the annular chamber
 1009 MICCA-Spray. The later can be expressed as:

$$1010 \quad \Delta f = 2f_{1A1L} \frac{v_\theta}{c} \quad (5.1)$$

1011 with v_θ , the tangential velocity, and c , the speed of sound determined for a burnt gas
 1012 temperature $T = 1500$ K. For the configuration at hand, one can estimate $v_\theta = 1.7$ m/s,
 1013 leading to $\Delta f = 3.5$ Hz, which is indeed below the frequency resolution.

REFERENCES

- 1014 AGUILAR J.G., DAWSON J.R., SCHULLER T., DUROX D., PRIEUR K., AND CANDEL S. 2021 Locking of azimuthal
 1015 modes by breaking the symmetry in annular combustors, *Combust. Flame*, **234**, p. 111639.
 1016 BAUERHEIM M., SALAS P., NICOU D., AND POINSO T. 2014 Symmetry breaking of azimuthal thermo-
 1017 acoustic modes in annular cavities: a theoretical study, *J. Fluid Mech.*, **760**, p. 431-465.
 1018 BAUERHEIM M., CAZALENS M., AND POINSO T. 2015 A theoretical study of mean azimuthal flow and

- 1019 asymmetry effects on thermo-acoustic modes in annular combustors, *In Proc. Combust. Inst.*, **35(3)**,
1020 p. 3219-3227.
- 1021 BAUERHEIM M., NDIAYE A., CONSTANTINE P., MOREAU S., AND NICOU D. 2016 Symmetry breaking of
1022 azimuthal thermoacoustic modes: the UQ perspective, *J. Fluid Mech.*, **789**, p. 534-566.
- 1023 BOTHIEN M.R., NOIRAY N., AND SCHUERMANS B. 2015 Analysis of azimuthal thermo-acoustic modes in
1024 annular gas turbine combustion chambers, *ASME J. Eng. Gas Turb. Power*, **137(6)**, p. 061505.
- 1025 BOUJO E., DENISOV A., SCHUERMANS B., AND NOIRAY N. 2016 Quantifying acoustic damping using flame
1026 chemiluminescence, *J. Fluid Mech.*, **808**, p. 245-257.
- 1027 BOURGOUIN J.-F., DUROX D., MOECK J.P., SCHULLER T., AND CANDEL S. 2013 Self-sustained instabilities in
1028 an annular combustor coupled by azimuthal and longitudinal acoustic modes, *In Proc. ASME Turbo
1029 Expo 2013*, Paper GT2013-95010.
- 1030 CAMPA G. AND CAMPOREALE S.M. 2014 Prediction of the thermoacoustic combustion instabilities in practical
1031 annular combustors, *ASME J. Eng. Gas Turb. Power*, **136(9)**, p. 091504.
- 1032 CANDEL S. 2002 Combustion dynamics and control: Progress and challenges, *Proc. Combust. Inst.*, **29(1)**,
1033 p. 1-28.
- 1034 DAWSON J.R. AND WORTH N.A. 2015 The effect of baffles on self-excited azimuthal modes in an annular
1035 combustor, *Proc. Combust. Inst.*, **35(3)**, p. 3283-3290.
- 1036 DOWLING A.P. 1997 Nonlinear self-excited oscillations of a ducted flame, *J. Fluid Mech.*, **346**, p. 271-290.
- 1037 DUROX D., SCHULLER T., AND CANDEL S. 2002 Self-induced instability of a premixed jet flame impinging
1038 on a plate, *Proc. Combust. Inst.*, **29(1)**, p. 69-75.
- 1039 DUROX D., SCHULLER T., NOIRAY N., BIRBAUD A.L., AND CANDEL S. 2009 Rayleigh criterion and acoustic
1040 energy balance in unconfined self-sustained oscillating flames, *Combust. Flame.*, **156**, p. 106-119.
- 1041 DUROX D., PRIEUR K., SCHULLER T., AND CANDEL S. 2015 Different flame patterns linked with swirling
1042 injector interactions in an annular combustor, *In Proc. ASME Turbo. Expo. 2015*, p. GT2015-42034.
- 1043 EVESQUE S. AND POLIFKE W. 2002 Low-order acoustic modelling for annular combustors: Validation and
1044 inclusion of modal coupling, *In Proc. ASME Turbo. Expo. 2002*, Paper GT2002-30064.
- 1045 EVESQUE S., POLIFKE W. AND PANKIEWITZ C. 2003 Spinning and azimuthally standing acoustic modes in
1046 annular combustors, *In Proc. 9th AIAA/CEAS Aeroacoustics Conference and Exhibit*, AIAA Paper
1047 2003-3182.
- 1048 FANACA D., ALEMELA P., ETTNER F., HIRSCH C., SATTELMAYER T., AND SCHUERMANS B. 2008 Determination
1049 and comparison of the dynamic characteristics of a perfectly premixed flame in both single and
1050 annular combustion chambers, *In Proc. ASME Turbo. Expo. 2008*, Paper GT2008-50781.
- 1051 FAURE-BEAULIEU A. AND NOIRAY N. 2020 Symmetry breaking of azimuthal waves: Slow-flow dynamics
1052 on the Bloch sphere, *Phys. Rev. Fluids*, **5(2)**, p. 023201.
- 1053 FISCHER, A. HIRSCH, C. AND SATTELMAYER, T. 2006 Comparison of multi-microphone transfer matrix
1054 measurements with acoustic network models of swirl burners. *J. Sound Vib.*, **298**, p. 73-83.
- 1055 GHIRARDO G. AND JUNIPER M.P. 2013 Azimuthal instabilities in annular combustors: standing and spinning
1056 modes, *Proc. R. Soc. A.*, **469(2157)**, p. 20130232.
- 1057 GHIRARDO G., ČOŠIĆ B., JUNIPER M.P., AND MOECK J.P. 2015 State-space realization of a describing
1058 function, *Nonlinear Dyn.*, **(82)**, p. 9-28.
- 1059 GHIRARDO G. AND BOTHIEN M.R. 2018 Quaternion structure of azimuthal instabilities, *Phys. Rev. Fluids*,
1060 **3(11)**, p. 113202.
- 1061 GHIRARDO G., NYGÅRD H.T., CUQUEL A., AND WORTH N.A. 2021 Symmetry breaking modelling for
1062 azimuthal combustion dynamics, *Proc. Combust. Inst.*, **38(4)**, p. 5953-5962.
- 1063 HAN X., LI J., AND MORGANS A.S. 2015 Prediction of combustion instability limit cycle oscillations by
1064 combining flame describing function simulations with a thermoacoustic network model, *Combust.
1065 Flame*, **(162)10**, p. 3632-3647.
- 1066 HUANG Y. AND YANG V. 2005 Effect of swirl on combustion dynamics in a lean-premixed swirl-stabilized
1067 combustor, *Proc. Combust. Inst.*, **30**, p. 1775-1782.
- 1068 HUANG Y. AND YANG V. 2009 Dynamics and stability of lean-premixed swirl-stabilized combustion, *Prog.
1069 Energy Combust. Sci.*, **(35)4**, p. 293-364.
- 1070 HUMBERT S.C., MOECK J.P., ORCHINI A., AND PASCHEREIT C.O. 2021 Effect of an azimuthal mean flow on the
1071 structure and stability of thermoacoustic modes in an annular combustor model with electroacoustic
1072 feedback, *ASME J. Eng. Gas Turb. Power*, **143(6)**, p. 061026.
- 1073 HUMBERT S.C., MOECK J.P., PASCHEREIT C.O., AND ORCHINI A. 2023 Symmetry-breaking in
1074 thermoacoustics: Theory and experimental validation on an annular system with electroacoustic
1075 feedback, *J. Sound Vib.*, **548**, p. 117376

- 1076 INDEKOFER T., AHN B., KWAH Y.H., WISEMAN S., MAZUR M., DAWSON J.R., AND WORTH N.A.. 2021 The
1077 effect of hydrogen addition on the amplitude and harmonic response of azimuthal instabilities in a
1078 pressurized annular combustor, *Combust. Flame*, **228**, p. 375-387.
- 1079 INDEKOFER T., FAURE-BEAULIEU A., DAWSON J.R., AND NOIRAY N. 2022 Spontaneous and explicit symmetry
1080 breaking of thermoacoustic eigenmodes in imperfect annular geometries, *J. Fluid Mech.*, **944**, p. A15.
- 1081 KOMAREK T. AND POLIFKE W. 2010 Impact of swirl fluctuations on the flame response of a perfectly premixed
1082 swirl burner., *ASME J. Eng. Gas Turb. Power*, **132**, p.061503.
- 1083 KOPITZ J., HUBER A., SATTELMAYER T., AND POLIFKE W. 2005 Thermoacoustic stability analysis of an
1084 annular combustion chamber with acoustic low order modeling and validation against experiment,
1085 *In Proc. ASME Turbo. Expo. 2005*, Paper GT2005-68797.
- 1086 KREBS W., FLOHR P., PRADE B., AND HOFFMANN S. 2002 Thermoacoustic stability chart for high-intensity
1087 gas turbine combustion systems, *Combust. Sci. Technol.*, **174(7)**, p. 99-128.
- 1088 LATOUR V., DUROX D., RAJENDRAM SOUNDARARAJAN P., RENAUD A., AND CANDEL S. 2023 Effects of
1089 fuel composition on azimuthal combustion instabilities in an annular combustor equipped with spray
1090 injectors, *In Proc. ASME Turbo. Expo. 2023*, Paper GT2023-101370.
- 1091 LATOUR V., RAJENDRAM SOUNDARARAJAN P., DUROX D., RENAUD A., AND CANDEL S. 2023 Assessing
1092 transfer matrix models and measurements using acoustic energy conservation principles, *Accepted
1093 for publication in ASME J. Eng. Gas Turb. Power*
- 1094 MAZUR M., NYGÅRD H.T., DAWSON J.R., AND WORTH N.A. 2019 Characteristics of self-excited spinning
1095 azimuthal modes in an annular combustor with turbulent premixed bluff-body flames, *Proc. Combust.
1096 Inst.*, **37(4)**, p. 5129-5136.
- 1097 MENS AH G.A., MAGRI L., ORCHINI A., AND MOECK J.P. 2019 Effects of asymmetry on thermoacoustic
1098 modes in annular combustors: a higher-order perturbation study., *ASME J. Eng. Gas Turb. Power*,
1099 **141(4)**, p. 041030.
- 1100 MOECK J.P., PAUL M., AND PASCHEREIT C.O. 2010 Thermoacoustic Instabilities in an annular Rijke tube, *In
1101 Proc. ASME Turbo. Expo. 2010*, Paper GT2010-23577.
- 1102 MUNJAL M.L. AND DOIGE A.G. 1990 Theory of a two source-location method for direct experimental
1103 evaluation of the four-pole parameters of an aeroacoustic element, *J. Sound Vib.*, **141(2)**, pp. 323-333
- 1104 NOIRAY N., DUROX D., SCHULLER T., AND CANDEL S. 2008 A unified framework for nonlinear combustion
1105 instability analysis based on the flame describing function, *J. Fluid Mech.*, **615**, p. 139-167.
- 1106 NOIRAY N., BOTHIEN M., AND SCHUERMANS B. 2011 Investigation of azimuthal staging concepts in annular
1107 gas turbines, *Combust. Theory Model.*, **15(5)**, p. 585-606.
- 1108 NOIRAY N. AND SCHUERMANS B. 2013 On the dynamic nature of azimuthal thermoacoustic modes in annular
1109 gas turbine combustion chambers, *Proc. R. Soc. A.*, **469(2151)**, p. 20120535.
- 1110 ORCHINI A., ILLINGWORTH S.J., AND JUNIPER M.P. 2015 Frequency domain and time domain analysis of
1111 thermoacoustic oscillations with wave-based acoustics, *J. Fluid Mech.*, **775**, p. 387-414.
- 1112 PALIÈS P., DUROX D., SCHULLER T., AND CANDEL S. 2011 Nonlinear combustion instability analysis based
1113 on the flame describing function applied to turbulent premixed swirling flames, *Combust. Flame*,
1114 **158(10)**, p. 1980-1991.
- 1115 PANKIEWITZ C. AND SATTELMAYER T. 2003 Time domain simulation of combustion instabilities in annular
1116 combustors., *ASME J. Eng. Gas Turb. Power*, **125(3)**, pp. 677-685.
- 1117 PARMENTIER J.-F., SALAS P., WOLF P., STAFFELBACH G., NICOU D., AND POINSOT T. 2008 A simple analytical
1118 model to study and control azimuthal instabilities in annular combustion chambers, *Combust. Flame*,
1119 **159(7)**, p. 2374-2387.
- 1120 PATAT C., BAILLOT F., BLAISOT J.-B., AND DOMINGUES E. 2021 Responses of lean swirling spray flames
1121 to acoustic pressure and transverse velocity perturbations, *In Proceedings of the Symposium on
1122 Thermoacoustics in Combustion: Industry meets Academia (SoTiC 2021), Munich*.
- 1123 POINSOT T. 2017 Prediction and control of combustion instabilities in real engines, *Proc. Combust. Inst.*,
1124 **36(1)**, p. 1-28.
- 1125 PRIEUR K., DUROX D., SCHULLER T., AND CANDEL S. 2017 A hysteresis phenomenon leading to spinning or
1126 standing azimuthal instabilities in an annular combustor, *Combust. Flame*, **175**, p. 283-291.
- 1127 RAJENDRAM SOUNDARARAJAN P., VIGNAT G., DUROX D., RENAUD A., AND CANDEL S. 2021 Effect of different
1128 fuels on combustion instabilities in an annular combustor, *ASME J. Eng. Gas Turb. Power*, **143(3)**,
1129 p. 031007.
- 1130 RAJENDRAM SOUNDARARAJAN P., DUROX D., RENAUD A., AND CANDEL S. 2022a Azimuthal instabilities
1131 of an annular combustor with different swirling injectors, *ASME J. Eng. Gas Turb. Power*, **144(11)**,
1132 p. 111018.

- 1133 RAJENDRAM SOUNDARARAJAN P., DUROX D., RENAUD A., VIGNAT G., AND CANDEL S. 2022*b* Swirler effects
1134 on combustion instabilities analyzed with measured FDFs, injector impedances and damping rates,
1135 *Combust. Flame*, **238**, p. 011016.
- 1136 SCHUERMANS B., GUETHE F., PENNELL D., GUYOT D., AND PASCHEREIT C.O. 2010 Thermoacoustic modeling
1137 of a gas turbine using transfer functions measured under full engine pressure, *ASME J. Eng. Gas*
1138 *Turb. Power*, **132(11)**, p. 111503.
- 1139 SCHULLER T., DUROX D., PALIES P, AND CANDEL S. 2012 Acoustic decoupling of longitudinal modes in
1140 generic combustion systems, *Combust. Flame*, **159**, pp. 1921-1931.
- 1141 SCHULLER T., POINSOT T., AND CANDEL S. 2020 Dynamics and control of premixed combustion systems
1142 based on flame transfer and describing functions, *J. Fluid Mech.*, **894**, P1-P95.
- 1143 STAFFELBACH G., GICQUEL L.Y.M., BOUDIER G., AND POINSOT T. 2009 Large Eddy Simulation of self excited
1144 azimuthal modes in annular combustors, *Proc. Combust. Inst.*, **32**, p. 2909-2916.
- 1145 STOW S.R. AND DOWLING A.P. 2003 Modelling of circumferential modal coupling due to Helmholtz
1146 resonators, *In Proc. ASME Turbo Expo 2003*, Paper GT2003-38168.
- 1147 VIGNAT G., DUROX D., PRIEUR K., AND CANDEL S. 2019 An experimental study into the effect of injector
1148 pressure loss on self-sustained combustion instabilities in a swirled spray burner, *Proc. Combust.*
1149 *Inst.*, **37(4)**, p. 5205-5213.
- 1150 VIGNAT G. 2020 Injection and combustion dynamics in swirled spray flames and azimuthal coupling in
1151 annular combustors, *PhD thesis, Université Paris-Saclay, France*
- 1152 VIGNAT G., RAJENDRAM SOUNDARARAJAN P., DUROX D., VIÉ A., RENAUD A., AND CANDEL S. 2021 A joint
1153 experimental and Large Eddy Simulation characterization of the liquid fuel spray in a swirl injector,
1154 *ASME J. Eng. Gas Turb. Power*, **143(8)**, p. 081019.
- 1155 WOLF P., STAFFELBACH G., GICQUEL L., MÜLLER J.-D., AND POINSOT T. 2012 Acoustic and Large Eddy
1156 Simulation studies of azimuthal modes in annular combustion chambers., *Combust. Flame*, (**159**)**11**,
1157 p. 3398-3413.
- 1158 WORTH N.A. AND DAWSON J.R 2013 Modal dynamics of self-excited azimuthal instabilities in an annular
1159 combustion chamber, *Combust. Flame*, **160(11)**, p. 2476-2489.
- 1160 WORTH N.A. AND DAWSON J.R 2017 Effect of equivalence ratio on the modal dynamics of azimuthal
1161 combustion instabilities, *Proc. Comb. Inst.*, **36(3)**, p. 3743-3751.